

APPLIED INFORMATION SYSTEMS RESEARCH (AISR) PROGRAM

**Final Report for S-13811-G**  
**Parallel-Processing Astronomical Image-Analysis Tools for *HST* and *SIRTF***

PI: Kenneth J. Mighell (National Optical Astronomy Observatory)

## 1 Introduction and Motivation: “Can you fit a banana?”

During the past decade, NASA’s astrophysical mission designers have been challenged by administrators to do more science with fewer dollars. The “faster-better-cheaper” paradigm of mission design has lead to many innovative mission concepts which achieve lower total mission cost at the price of having some distortion in the optical design of instruments and/or telescopes. One way of compensating for distorted optics is to do more image processing with clever algorithms.

Technology Readiness Level (TRL) [34] enhancement programs, like the Applied Information Systems Research (AISR) program, can significantly help NASA’s astrophysical mission designers by promoting the development of new image processing algorithms from a basic technology research level (e.g., TR Levels 1–3) to the point where mission designers can consider using these new image processing algorithms in future NASA missions (e.g., TR Levels 5–6). Space-based demonstration of new technologies is clearly beyond the scope and means of AISR, yet AISR can develop new applied information systems technologies which would be excellent candidates for consideration for use in demonstrator programs like the New Millennium Program [29] which tests advanced technology for use in space flight.

One of the early design concepts for the 8-m *Next Generation Space Telescope* (NGST), currently known as the 6.5-m *James Webb Space Telescope* (JWST), had a very elliptical primary mirror in order to fit it into a 4-m diameter launch shroud. John Mather, the NGST Project Scientist, described this concept to the Principal Investigator (PI) in January 1999 at the 193rd meeting of the American Astronomical Society (AAS) in Austin, Texas. Mather explained that the downside of the elliptical primary mirror design was the fact that the oddly shaped primary mirror would cause stars to be shaped like bananas. Mather asked the PI: “Can you fit a banana?” The PI answered: “Yes.” As there was no clear consensus within the NGST project in 1999 whether accurate stellar photometry and astrometry was theoretically and/or practically possible with complex distorted Point Spread Functions (PSFs), Mather replied: “Prove it!”

With support of the two-year AISR grant S-13811-G, the PI has now met Mather’s challenge by proving that precise and accurate stellar photometry and astrometry is possible and practical with ugly space-based PSFs which have high spatial frequencies rarely seen in ground-based astronomy due to the blurring of the Earth’s atmosphere. The PI has recently demonstrated [24] that the current C implementation of his MATPHOT algorithm [12] [1] can achieve millipixel relative astrometry and millimag photometric precision with complicated space-based discrete Point Spread Functions imaged onto imperfect detectors with large intrapixel quantum efficiency variations.

## 2 AISR Grant S-13811-G Results

### 2.1 QLWFPC2: Quick-Look WFPC2 Stellar Photometry

The PI wrote a parallel-processing stellar photometry code called QLWFPC2 [31] [20] [19] which was designed to do quick-look analysis of two entire WFPC2 (Wide Field Planetary Camera 2) [2] observations from the *Hubble Space Telescope (HST)* in under 5 seconds using a fast Beowulf cluster with a Gigabit Ethernet local network. This program is written in ANSI C and uses the MPICH [28] implementation of the Message Passing Interface (MPI) [27] for the parallel-processing communications, the CFITSIO [3] library (from HEASARC at NASA's Goddard Space Flight Center) for reading the FITS [4] standard files from the *Hubble Space Telescope* Data Archive [7], and the Parameter Interface Library (PIL) [30] (from the INTEGRAL Science Data Center) for the IRAF [8] parameter-file user interface. Stellar instrumental (flight-system) magnitudes are converted to standard colors using the color-transformation equations of the *HST* WFPC2 Team [5].

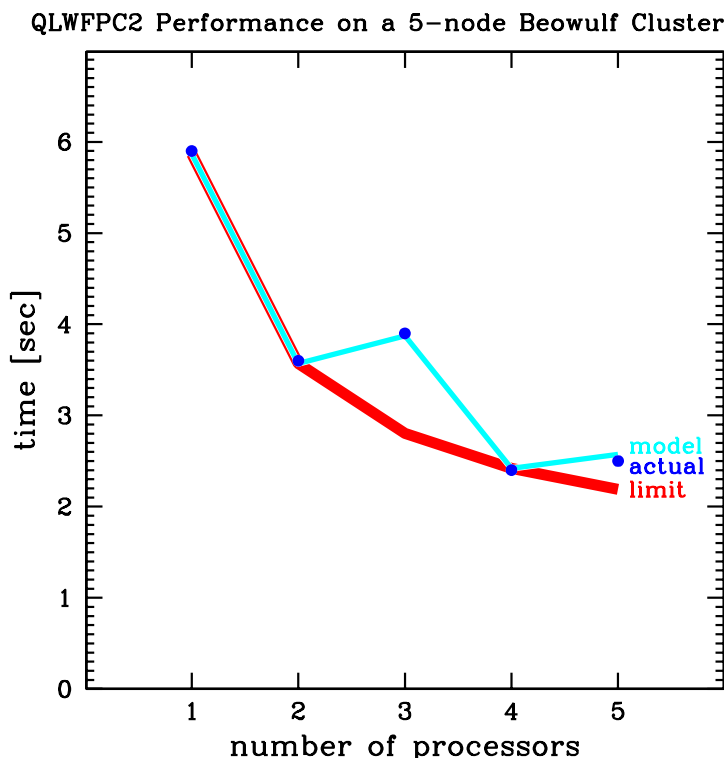


Figure 1. Typical QLWFPC2 performance.

QLWFPC2 running on four 1.8-GHz processors takes about 2.4 seconds (see **Figure 1**) to analyze the WFPC2 archive datasets u37ga407r.c0.fits (F555W; 300 s) and u37ga401r.c0.fits (F814W; 300 s) of M54 (NGC 6715) which is the bright massive globular cluster near the center of the nearby Sagittarius dwarf spheroidal galaxy (see **Figure 2**).

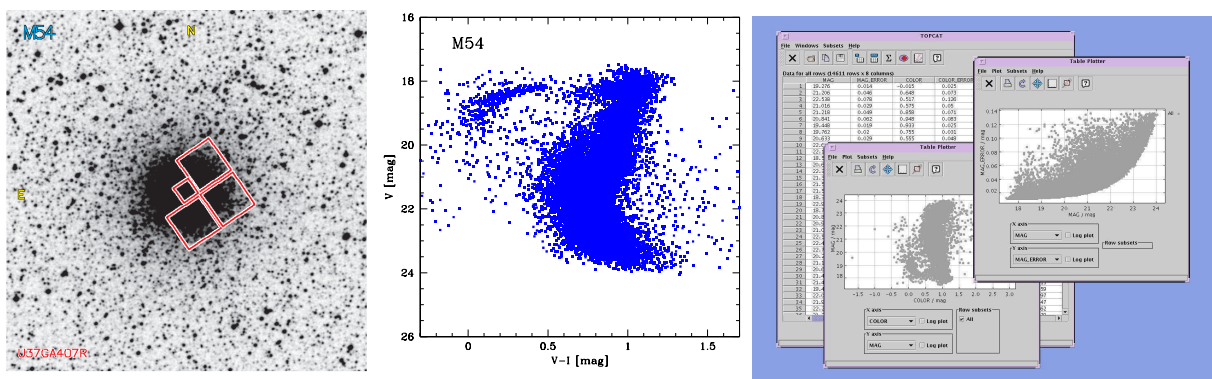


Figure 2. QWFPC2 analysis of M54.

By default QWFPC2 stellar photometry of M54 results are given in a human-readable ASCII text which can be easily transformed into a color-magnitude diagram using publication-grade graphics packages like SuperMongo [33] (middle figure of Fig. 2). QWFPC2 also produces XML output files that are compliant with the U.S. National Virtual Observatory [36] VOTable standard [37]; the QWFPC2 XML output files can be viewed with Java-based VOTable viewers like Starlink's TOPCAT [35] (right figure of Fig. 2).

Six F555W filter observations of M54 were obtained for the *HST* observing program GO-6701 (PI: Ibata). QWFPC2 was run on all 15 pair combinations of the F555W observations; **more than one million stars were analyzed in 42 seconds of wall-clock time**. Searching for evidence of significant variability in the magnitudes of individual stars lead to the serendipitous discovery [32][26] of many new variable stars in the central region of this extragalactic star cluster — a region where no variables have been reported by previous ground-based studies (see **Figure 3**). Stars exhibiting significant variability are shown with large squares. Helium-burning RR Lyrae candidates are expected to be found in the gray region of the magnitude- $\Delta$ magnitude diagram on the left and most of the variable stars found with this quick-look time-domain QWFPC2 analysis are found at the expected location for RR Lyraes on M54's horizontal-branch in the color-magnitude diagram on the right. Many of the fainter variable candidates are likely to be eclipsing binaries.

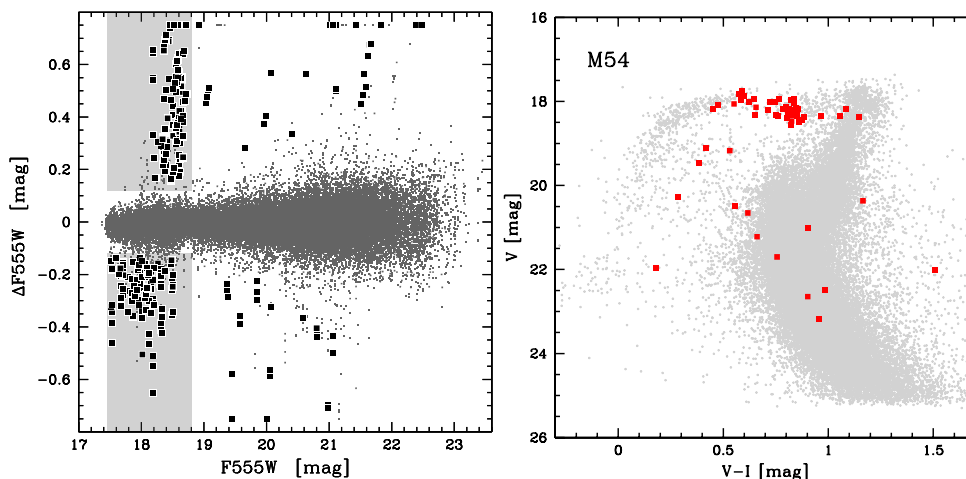


Figure 3. Discovery of variable stars in the central region of M54 using QWFPC2.

This discovery is an example of how QLWFPC2 can be used to quickly explore the time domain of observations in the *HST* Data Archive. **The PI and Roederer [25] used QLWFPC2 to discover flickering red giants in the nearby Ursa Minor dwarf spheroidal galaxy.**

Reading two *HST* WFPC2 datasets and writing 5 megabytes of output on a 7200-rpm NFS-mounted disk takes about one second of the typical 2.4 s total execution time. Excluding disk I/O, **QLWFPC2 analyzes about 10,000 stars per second per filter per CPU GHz.**

Figure 1 shows typical QLWFPC2 performance results with two WFPC2 observations of a Local Group globular cluster running on the PI's research development 5-node Beowulf cluster with 1.8-GHz AMD Athalon CPUs and a Gigabit Ethernet local network. The *thin line* of Fig. 1 shows a simple performance model based on measured cluster performance metrics (network bandwidth, disk drive bandwidth, and execution time of QLWFPC2 with a single CPU). The *thick line* shows the theoretical limit of performance. Note that the current version of the QLWFPC2 algorithm already meets the ideal performance values for 1, 2, and 4 processors. A single WFPC2 dataset is about 10 Mbytes in size and is partitioned into four calibrated images from the PC1, WF2, WF3, and the WF4 cameras; the current QLWFPC2 analysis algorithm sends all of the image data from one WFPC2 camera to a single compute (slave) node for analysis — the increase in computation time for 3 (5) processors compared to 2 (4) processors reflects the underlying 4-fold partitioning of a single WFPC2 dataset [38]. Spreading the analysis of data from a WFPC2 camera to all compute nodes would improve the computation time for 3 and 5 (and more) processors but would not improve the results for 1, 2 and 4 processors which are already optimal.

**Gigabit Ethernet was the critical cluster parameter for achieving the AISR project design goal of typical execution times of significantly less than 5 seconds.** Fast Ethernet would have been too slow since the time penalty for transmitting the data over Fast Ethernet would have exceeded the computation time required for a single CPU.

## 2.2 MATPHOT: Photometry & Astrometry with Discrete PSFs

The PI has developed a C-language implementation of his MATPHOT algorithm for precise and accurate stellar photometry and astrometry with discrete PSFs [24] [23] [22] [21] [18] [17] [16] [15] [14]. The MATPHOT code uses discrete (sampled) Point Spread Functions consisting of a numerical table represented by a matrix in the form of a FITS [4] image. Discrete PSFs are shifted within an observational model using a 21-pixel-wide damped sinc function,

$$f^{\text{shifted}}(x_0) \equiv \sum_{i=-10}^{10} f(x_i) \frac{\sin(\pi(x_i - x_0))}{\pi(x_i - x_0)} \exp\left(-\left[\frac{x_i - x_0}{3.25}\right]^2\right), \quad (1)$$

and position partial derivatives are computed using a five-point numerical differentiation formula,

$$f'(x_i) \approx \frac{1}{12} [f(x_{i-2}) - 8f(x_{i-1}) + 8f(x_{i+1}) - f(x_{i+2})], \quad (2)$$

[24]. Precise and accurate stellar photometry and astrometry are achieved with undersampled CCD observations by using supersampled discrete PSFs that are sampled 2, 3, or more times more finely than the observational data. Although these numerical techniques are not mathematically perfect, they are sufficiently accurate for precision stellar photometry and astrometry due to photon noise which is present in all astronomical imaging observations [24] [22] [21]. The current

implementation [12] [1] of the MATPHOT algorithm is based on a robust implementation of the Levenberg-Marquardt method of nonlinear least-squares minimization [10] [11] [13] [14]. Detailed analysis of simulated *Next Generation Space Telescope* (NGST) observations demonstrate that millipixel relative astrometry and millimag photometric precision is achievable with complicated space-based discrete PSFs [24].

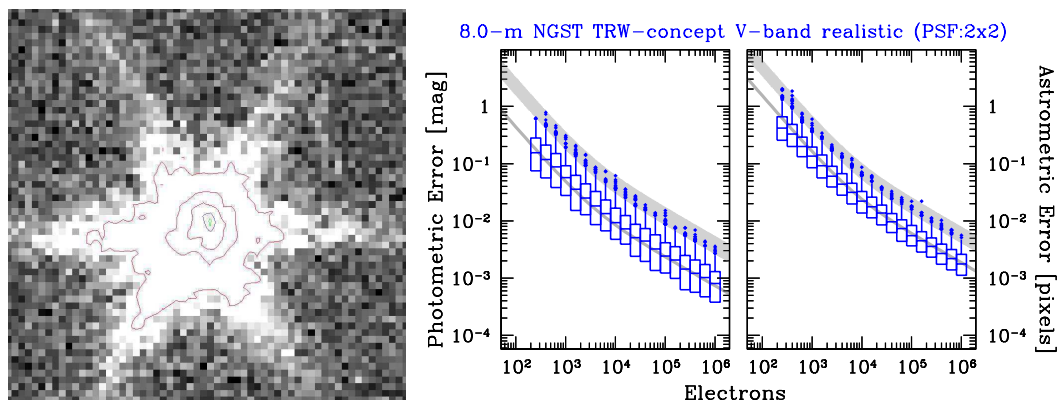


**Figure 4.** MATPHOT analysis of 10,000 simulated NGST stellar observations.

A simulated *NGST* V-band stellar observation with the 8-meter TRW-concept 1.5-micron diffraction-limited primary mirror is shown in **Figure 4** with the 90%, 50%, 10%, 1%, and 0.1% contours relative to the peak intensity. The pixel scale is  $0.0128 \text{ arcsec pixel}^{-1}$ . The original version of this PSF was kindly provided by John Krist at the Space Telescope Science Institute (STScI). The right side of Fig. 4 shows the MATPHOT-based analysis of 10,000 simulated *NGST* V-band CCD observations of stars with true flux values between 250 and  $10^6$  electrons (photons). Each observation was simulated with a  $2 \times 2$  supersampled *NGST* PSF located near the center of  $60 \times 60$  pixels on a flat background of 100 electrons ( $e^-$ ) with a CCD readout noise level of  $3 e^- \text{ pixel}^{-1}$ . The results are plotted using box-and-whisker plots to better display the statistical range of recovered values for photometry and astrometry. **Figure 5** shows similar results for simulated 6.5-m *James Webb Space Telescope* (JWST) observations with a perfect one-micron PSF (shown with a log stretch to better display the higher spatial frequencies).

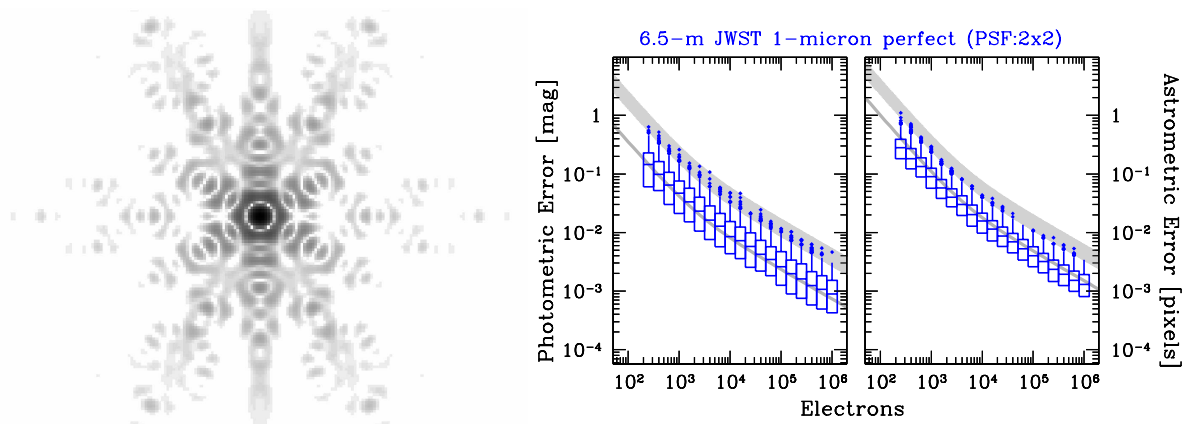


**Figure 5.** MATPHOT analysis of 10,000 simulated JWST stellar observations.

A major result of this AISR grant has been the development of a **theoretical photometric and astrometric performance model for PSF-fitting stellar photometry and astrometry**; the PI has demonstrated that his MATPHOT algorithm achieves the Cramér-Rao Lower Bounds for stellar photometry and astrometry [24]. The PI has implemented a standalone version of his MATPHOT algorithm in C as part of his AISR project and all of the source code and documentation is available to the general space-science community at a dedicated web site at NOAO [12] and at the AISRP Code Archive Server [1]. The *solid curves* in Figs. 4 and 5 show the predicted **median** performance of the MATPHOT algorithm for these simulations; note that the actual median values (central bars in the boxes) lie on top or very near the performance model prediction. The *gray bands* in the above photometric (astrometric) error plots show the **predicted outlier region** for  $2.3\sigma$  ( $3.0\sigma$ ) to  $5.0\sigma$  outliers (shown as points above the top whisker in Figs. 4 and 5). Note how well the theoretical performance model agrees with the actual MATPHOT measurements — even with these very complicated (simulated) space-based discrete PSFs.

Current infrared detector technology can produce imagers with non-uniform pixel response functions. The left side of **Figure 6** shows the non-uniform pixel response function of the *Hubble Space Telescope's* NIC3 camera with the F160W filter (centered at 1.6 microns) as determined by Lauer [9]; white indicates an excess of 0.12 mag and black is a 0.09 mag deficit. The right side of Fig. 6 shows the variation of **measured brightness of a single star** as observed in 136 separate dithered images of the HDF-S NICMOS field using the NIC3 camera with the F160W filter (plotted as a function of subpixel distance of the center of the star from the center of the pixel) [6]. Significant flux loss due to non-uniform intrapixel pixel response functions is clearly an observational fact in some existing space-based astronomical cameras.

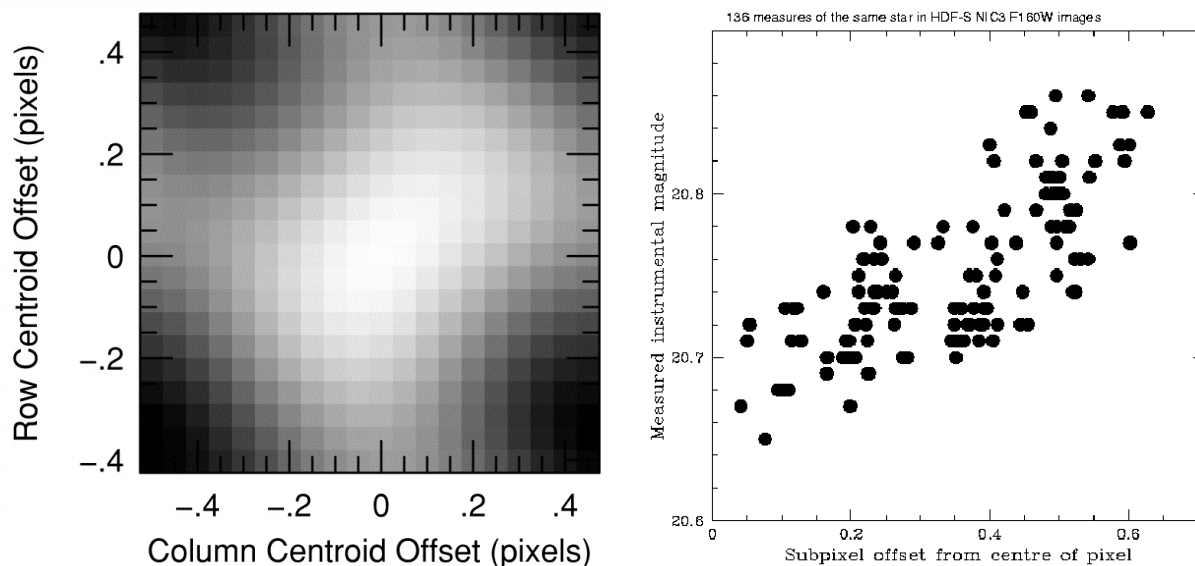


**Figure 6.** *HST* NIC3 F160W Non-Uniform Pixel Response Function.

An experimental version of MATPHOT was created to simulate such an IR detector; a pixel was split into 16 subpixels and all the subpixels in the first row and column were declared to be gate structures with zero efficiency converting photons to electrons and the other nine subpixels had 100% conversion efficiency. Note that only 56% of the total pixel area was optically active.

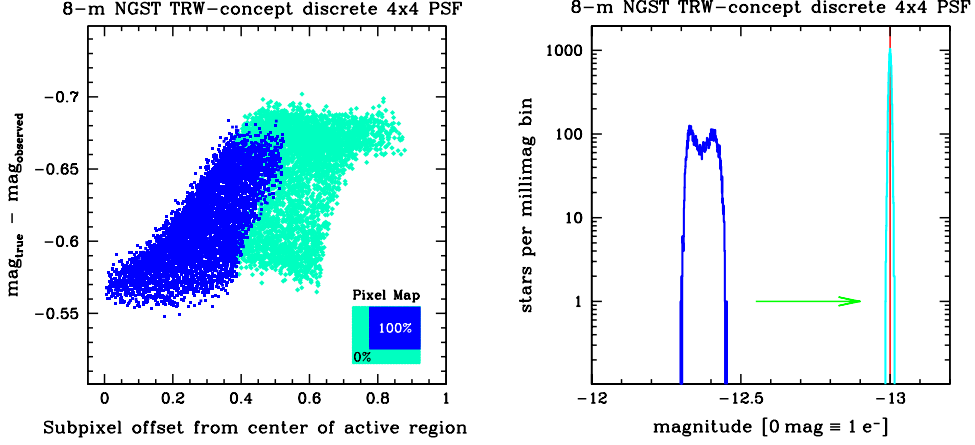


Figure 7. MATPHOT experiment with a large intrapixel quantum efficiency variation.

Ten thousand CCD stellar observations of  $-13$  mag stars ( $\sim 2.512^{13}$  photons) were simulated and analyzed with the experimental version of MATPHOT using a  $4 \times 4$  supersampled version of the simulated  $V$ -band *NGST* PSF described above.

The optically inactive gate structures of the pixel cause the observed number of electrons in each stellar image to be significantly less than the number of photons which fell on the detector. **The total amount of loss was dependent on where the center of the star fell within the central pixel of the stellar image.** The left side of **Figure 7** shows that stars centered in the middle of the active area of a pixel suffered a  $\sim 40\%$  loss ( $\Delta m \approx 0.56$  mag) while those centered on gate structures lost up to  $47\%$  ( $\Delta m \approx 0.69$  mag) [24].

The mean *observed* stellar magnitude for these  $-13$  mag stars was  $-12.3728 \pm 0.0359$  mag. The photometric performance model predicts an rms measurement error of  $0.0036$  mag for these bright stars. With an average loss of  $44\%$  and an rms measurement error that is *ten times larger* than expected from photon statistics, the *observed* stellar magnitudes were clearly neither precise or accurate (left histogram on the right side of Fig. 7).

The mean *measured* stellar magnitude reported by the experimental version of MATPHOT was  $-12.9998 \pm 0.0039$  mag and the mean rms error estimated by the program was  $0.00384 \pm 0.00006$  mag (right histogram on the right side of Fig. 7). The photometric performance of the experimental version of MATPHOT is fully consistent with theoretical expectations — which were derived for an ideal detector with no intrapixel QE variation.

The experimental version of MATPHOT was able to do an excellent job in recovering the true stellar magnitude of the 10,000  $-13$  mag stars — despite being presented with a worst-case scenario of undersampled observations with an ugly PSF imaged on an ugly detector with a very large intrapixel QE variation [24].

**Excellent stellar photometry and astrometry is possible with ugly PSFs imaged onto ugly detectors as long as the image formation process *within the detector* is accurately modeled by the photometric reduction code.**

## References

- [1] AISR Code Archive Server web site:  
<http://astrophysics.arc.nasa.gov/~pgazis/CodeArchiveServer.html>
- [2] *WFPC2 Instrument Handbook (Version 6.0)*,  
Biretta, J., et al. 2001, (Baltimore: STScI)
- [3] CFITSIO website: <http://heasarc.gsfc.nasa.gov/docs/software/fitsio>
- [4] FITS Support Office: <http://fits.gsfc.nasa.gov>
- [5] *The Photometric Performance and Calibration of WFPC2*,  
Holtzman, J. A., Burrows, C. J., Casertano, S. Hester, J. J., Trauger, J. T., Watson, A. M., &  
Worthey, G. 1995, PASP, 107, 1065,
- [6] *Dithering, Sampling and Image Reconstruction*,  
Hook, R. N., & Fruchter, A. S. 2000,  
in *Astronomical Data Analysis Software and Systems IX*, ASP Conference Series, Vol. 216, edited by N.  
Manset, C. Veillet, D. Crabtree (ASP: San Francisco: ASP), 521
- [7] *Hubble Space Telescope Data Archive*: <http://archive.stsci.edu/hst>
- [8] IRAF website: <http://iraf.noao.edu>
- [9] *The Photometry of Undersampled Point-Spread Functions*,  
Lauer, T. R. 1999, PASP, 111, 1434
- [10] *A Method for the Solution of Certain Problems in Least Squares*,  
Levenberg, K. 1944, Q. App. Math., 2, 164
- [11] *An Algorithm for Least-Squares Estimation of Nonlinear Parameters*,  
Marquardt, D. 1963, J. SIAM, 11, 431
- [12] MATPHOT web site: <http://www.noao.edu/staff/mighell/matphot/>
- [13] *Accurate stellar photometry in crowded fields*,  
Mighell, K. J. 1989, MNRAS, 238, 807
- [14] *Algorithms for CCD Stellar Photometry*  
Mighell, K. J. 1999 (30-min review talk, 1998 November 3),  
in *Astronomical Data Analysis Software and Systems VIII*, ASP Conference Series, Vol. 172., edited by  
D. M. Mehringer, R. L. Plante, and D. A. Roberts (ASP: San Francisco), 317
- [15] *The MATPHOT Algorithm for Digital Point Spread Function CCD Stellar Photometry*,  
Mighell, K. J. 2002 (invited 15-min talk, 2001 October 2),  
in *Astronomical Data Analysis Software and Systems XI*, ASP Conference Series, Vol. 281, edited by  
D. Bohlender, D. Durand, and T. H. Handley (ASP, San Francisco), 387



## REFERENCES

---

- [16] *The MATPHOT algorithm for digital point spread function CCD stellar photometry*,  
Mighell, K. J. 2002 (invited 20-min talk, 2002 August 27),  
in *Astronomical Data Analysis II* (2002 August 27-28, Waikoloa, HI), *Proceedings of SPIE*, Vol. 4847,  
207 (<http://www.spie.org/Conferences/Programs/02/as/confs/4847.html>)
- [17] *The MATPHOT algorithm for digital point spread function CCD stellar photometry*,  
Mighell, K. J. 2002 (invited 20-min talk, 2002 September 20),  
in *Proceedings of the 2002 AMOS Technical Conference*, Maui, 2002 September 16–20  
([http://www.maui.afmc.af.mil/AMOS02\\_Program.pdf](http://www.maui.afmc.af.mil/AMOS02_Program.pdf))
- [18] *A Theoretical Photometric and Astrometric Performance Model for Point Spread Function CCD Stellar Photometry*,  
Mighell, K. J. 2003,  
in *Astronomical Data Analysis Software and Systems XII*, *ASP Conference Series*, Vol. 295, edited by  
H. E. Payne, R. I. Jedrzejewski, and R. N. Hook (ASP, San Francisco), 395
- [19] *QLWFPC2: Parallel-Processing Quick-Look WFPC2 Stellar Photometry based on the Message Passing Interface*,  
Mighell, K. J. 2003, *BAAS*, 35, 1207  
(poster # 4.01, 203rd AAS meeting, 2004 January 5, Atlanta),  
abstract: <http://www.aas.org/publications/baas/v35n5/aas203/161.htm>
- [20] *QLWFPC2: Parallel-Processing Quick-Look WFPC2 Stellar Photometry Based on the Message Passing Interface*,  
Mighell, K. J. 2004,  
in *Astronomical Data Analysis Software and Systems XIII* (2003 October 12–15, Strasbourg), *ASP Conference Series*, edited by F. Ochsenbein, M. Allen, and D. Egret (ASP, San Francisco), 4 page article (in press)
- [21] *Mathematical Challenges of using Point Spread Function Analysis Algorithms in Astronomical Imaging*,  
Mighell, K. J. 2004 (50-min review talk, 2004 January 27),  
*Mathematical Challenges in Astronomical Imaging (AI2004)*,  
held at the Institute of Pure and Applied Mathematics, University of California, Los Angeles, 2004  
January 26–30 ([http://www.ipam.ucla.edu/publications/ai2004/ai2004\\_4544.pdf](http://www.ipam.ucla.edu/publications/ai2004/ai2004_4544.pdf))
- [22] *Photometric and Astrometric Accuracy Limits for Adaptive Optics Point Spread Functions*,  
Mighell, K. J. 2004 (30-min talk, 2004 May 10),  
*Center for Adaptive Optics (CfAO) Workshop on Adaptive Optics PSF Reconstruction*  
held at the Herzberg Institute of Astrophysics, Victoria, B.C., Canada, 2004 May 10–12  
([http://cfao.ucolick.org/meetings/psf\\_reconstruction/pdf/mighell.pdf](http://cfao.ucolick.org/meetings/psf_reconstruction/pdf/mighell.pdf))
- [23] *The MATPHOT Algorithm for Accurate and Precise Stellar Photometry and Astrometry Using Discrete Point Spread Functions*,  
Mighell, K. J. 2004, *BAAS*, 36, 1603  
(poster # 153.09, 205th AAS meeting, 2005 January 13, San Diego),  
(abstract: <http://www.aas.org/publications/baas/v36n5/aas205/920.htm> )

## REFERENCES

---

- [24] *Stellar Photometry and Astrometry with Discrete Point Spread Functions*  
Mighell, K. J. 2005, MNRAS, 361, 861
- [25] *Flickering Red Giants in the Ursa Minor Dwarf Spheroidal Galaxy:  
Detection of Low-Amplitude Variability in Faint Red Giant Branch Stars on 10 Minute Timescales*,  
Mighell, K. J., & Roederer, I. U. 2004, ApJ, 617, L41
- [26] Mighell, K. J. , & Schlafman, K. C. 2004, ApJL, (in preparation)
- [27] MPI website: <http://www-unix.mcs.anl.gov/mpi>
- [28] MPICH website: <http://www-unix.mcs.anl.gov/mpi/mpich>
- [29] New Millenium Program website: <http://nmp.jpl.nasa.gov>
- [30] PIL website: Retrieve OSA\_SW at <http://isdc.unige.ch/?Soft+download>
- [31] QWFPC2 website: <http://www.noao.edu/staff/mighell/qlwfp2>
- [32] *Serendipitous Discovery of Variable Stars in WFPC2 Observations of the Central Region of the Globular Cluster M54*,  
Schlafman, K. C., & Mighell, K. J. 2003, BAAS, 35, 1290  
(poster # 52.11, 203rd AAS meeting, 2004 January 6, Atlanta),  
abstract: <http://www.aas.org/publications/baas/v35n5/aas203/69.htm>
- [33] SuperMongo website: <http://www.astro.princeton.edu/~rhl/sm>
- [34] Technology Readiness Levels: [http://ranier.hq.nasa.gov/sensors\\_page/background/techlevels.html](http://ranier.hq.nasa.gov/sensors_page/background/techlevels.html)
- [35] TOPCAT website: <http://www.star.bris.ac.uk/~mbt/topcat>
- [36] U.S.National Virtual Observatory website: <http://www.us-vo.org>
- [37] VOTable website: <http://www.us-vo.org/news/votable.html>
- [38] WFPC2 field-of-view:  
[http://www.stsci.edu/instruments/wfpc2/Wfpc2\\_hand\\_current/ch1\\_introduction2.html#442625](http://www.stsci.edu/instruments/wfpc2/Wfpc2_hand_current/ch1_introduction2.html#442625)

# Stellar photometry and astrometry with discrete point spread functions

Kenneth J. Mighell<sup>★</sup>

*National Optical Astronomy Observatory, 950 North Cherry Avenue, Tucson, AZ 85719, USA*

Accepted 2005 May 19. Received 2005 April 22; in original form 2004 November 4

## ABSTRACT

The key features of the MATPHOT algorithm for precise and accurate stellar photometry and astrometry using discrete point spread functions (PSFs) are described. A discrete PSF is a sampled version of a continuous PSF, which describes the two-dimensional probability distribution of photons from a point source (star) just above the detector. The shape information about the photon scattering pattern of a discrete PSF is typically encoded using a numerical table (matrix) or an FITS (Flexible Image Transport System) image file. Discrete PSFs are shifted within an observational model using a 21-pixel-wide damped sinc function, and position-partial derivatives are computed using a five-point numerical differentiation formula. Precise and accurate stellar photometry and astrometry are achieved with undersampled CCD (charge-coupled device) observations by using supersampled discrete PSFs that are sampled two, three or more times more finely than the observational data. The precision and accuracy of the MATPHOT algorithm is demonstrated by using the C-language MPD code to analyse simulated CCD stellar observations; measured performance is compared with a theoretical performance model. Detailed analysis of simulated *Next Generation Space Telescope* observations demonstrate that millipixel relative astrometry and mmag photometric precision is achievable with complicated space-based discrete PSFs.

**Key words:** methods: analytical – methods: numerical – methods: statistical – techniques: image processing – techniques photometric – astrometry.

## 1 INTRODUCTION

A point spread function (PSF) is a continuous two-dimensional probability-distribution function that describes the scattering pattern of photons from a point source (star).

Encoding a PSF as a continuous mathematical function works well for many ground-based astronomical observations due to the significant blurring caused by turbulence in the Earth's atmosphere and dome/telescope seeing. Ground-based PSFs are typically characterized by having a lot of power in their spatial-frequency distributions at low spatial frequencies.

Space-based PSFs frequently have significant amounts of power at higher spatial frequencies due to the lack of blurring caused by atmospheric turbulence. Adaptive optics can produce PSFs with characteristics found in both uncorrected ground-based PSFs and space-based PSFs: low-spatial-frequency features (e.g. broad haloes) are frequently combined with high-spatial-frequency features (e.g. due to segmented mirrors).

Some PSF-fitting stellar photometric reduction programs describe the PSF as a combination of continuous mathematical functions and a residual matrix that contains the difference between the mathematical model of the PSF and an observed (true) PSF. This artificial

breaking of the PSF into analytical and discrete components is not without mathematical risk. Such residuals can have small features, which are described with higher spatial frequencies than are present in the actual observational data – a problem that can usually be mitigated by sampling residuals at higher spatial resolutions than the observational data.

What if we dispose of the use of continuous mathematical functions to model *any* part of the PSF and just use a matrix to describe *all* of the PSF? Is precise and accurate stellar photometry and astrometry possible using matrix PSFs with oversampled stellar image data? If that is possible, then what extra information, if any, is required in order to do precision photometric reductions with matrix PSFs on undersampled data?

This article describes how precise and accurate stellar photometry may be obtained using PSFs encoded as a matrix. The following section derives the theoretical performance limits of PSF-fitting stellar photometry and astrometry. Some of the key features of the MATPHOT algorithm are presented in Section 3. A demonstration computer program, called MPD, based on the current implementation of the MATPHOT algorithm, is described in Section 4. Simulated CCD (charge-coupled device) stellar observations are analysed with MPD in Section 5 and the performance of the MATPHOT algorithm is compared with theoretical expectations. Concluding remarks are given in Section 6. An appendix explains box-and-whisker plots, which are used extensively in this article.

<sup>★</sup>E-mail: mighell@noao.edu

## 2 THEORETICAL PERFORMANCE LIMITS

### 2.1 Point response functions

A point response function (PRF),  $\Psi$ , is the convolution of a PSF,  $\phi$ , and a detector response function (DRF),  $\Lambda$ :

$$\Psi \equiv \phi * \Lambda. \quad (1)$$

The PSF describes the two-dimensional distribution of *photons* from a star *just above the detector*. Although stellar photons are distributed as a point source above the Earth's atmosphere, a stellar image becomes a two-dimensional distribution as the stellar photons are scattered by atmospheric turbulence. The blurred stellar image is then further degraded by passage of the stellar photons through the combined telescope and camera optical elements (such as mirrors, lenses, apertures, etc.). The PSF is the convolution of all these blurring effects on the original point-source stellar image. The two-dimensional discrete (sampled) DRF describes how the detector electronics convert stellar photons ( $\gamma$ ) to electrons ( $e^-$ ) – including such effects as the diffusion of electrons within the detector substrate or the reflection (absorption) of photons on (in) the gate structures of the detector electronics.

The PSF is a two-dimensional probability-distribution function describing the scattering pattern of a photon. The volume integral of the PSF is 1:  $V_{\text{PSF}} \equiv 1$ ; photons, after all, have to be scattered *somewhere*. It is important to note that since the angular extent of a PSF can be quite large, the volume integral the PSF *over any given observation* is frequently less than 1 due to the limited spatial coverage of the observation.

The volume integral of a PRF is, by definition, 1 or less

$$V \equiv \iint_{-\infty}^{+\infty} \Psi \, dx \, dy = \iint_{-\infty}^{+\infty} (\phi * \Lambda) \, dx \, dy \leq 1, \quad (2)$$

where a value of less than 1 indicates a loss of stellar photons during the detection/conversion process within the detector. While the quantum efficiency (QE) variations within a single detector are generally not a major problem with state-of-the-art CCDs, intrapixel QE variations can be significant with some near-infrared detector technologies currently being used in astronomical cameras (e.g. Lauer 1999; Hook & Fruchter 2000).

A perfect DRF gives a PRF that is a *sampled version* of the PSF

$$\Psi_i \equiv \int_{x_i-0.5}^{x_i+0.5} \int_{y_i-0.5}^{y_i+0.5} \phi(x, y) \, dx \, dy, \quad (3)$$

where the  $i$ th pixel of the PRF located at  $(x_i, y_i)$  is the volume integral of the PSF over the area of the  $i$ th pixel. The actual limits of the above volume integral reflect the appropriate mapping transformation of the  $x$  and  $y$  coordinates onto the CCD pixel coordinate system.

The sharpness of a PRF is defined as the volume integral of the *square* of the *normalized* PRF

$$\text{sharpness} \equiv \iint_{-\infty}^{+\infty} \tilde{\Psi}^2 \, dx \, dy = \iint_{-\infty}^{+\infty} \left( \frac{\Psi}{V} \right)^2 \, dx \, dy. \quad (4)$$

Physically, sharpness is a shape parameter that describes the ‘pointiness’ of a PRF; sharpness values range from a maximum of 1 (all of the stellar flux is found within a single pixel) to a minimum of 0 (a flat stellar image). For example, cameras that are out of focus have broad PSFs with sharpness values near zero. A normalized

Gaussian PSF with a standard deviation of  $S$  pixels,

$$g(x, y; \mathcal{X}, \mathcal{Y}, S) \equiv \frac{1}{2\pi S^2} \exp \left[ -\frac{(x - \mathcal{X})^2 + (y - \mathcal{Y})^2}{2S^2} \right], \quad (5)$$

that has been *oversampled* with a perfect DRF will have a sharpness value of

$$\iint_{-\infty}^{+\infty} g^2(x, y; \mathcal{X}, \mathcal{Y}, S) \, dx \, dy = \frac{1}{4\pi S^2}. \quad (6)$$

A critically sampled normalized Gaussian PRF has a sharpness of  $1/(4\pi)$  and any PRF with a sharpness value greater than that value ( $\sim 0.0796$ ) can be described as being undersampled. Diffraction-limited optics, theoretically, give sharpness values that decrease (i.e. PSFs become flatter) with increasing photon wavelength – for a fixed pixel (detector) size. With real astronomical cameras, the value of sharpness frequently depends on where the centre of a star is located within the central pixel of the stellar image. For example, the *Hubble Space Telescope* (HST) WFPC2 Planetary Camera PRF at a wavelength of 200 nm has an observed sharpness value of 0.084 if the PRF is centred in the middle of a PC pixel or 0.063 if the PRF is centered on a pixel corner (table 6.5 of Biretta et al. 2001); at 600 nm the observed sharpness values range from 0.066 (pixel centred) to 0.054 (corner centered). The wide-field cameras of the HST WFPC2 instrument have pixels that are approximately half the angular resolution of the PC camera pixels; stellar images on the WF cameras are undersampled and the observed range of WF camera sharpness values are 0.102–0.120 at 200 nm and 0.098–0.128 at 600 nm.

The *effective background area*,  $\beta$ , of a PRF is defined as the *reciprocal* of the volume integral of the *square* of the PRF

$$\beta \equiv \left[ \iint_{-\infty}^{+\infty} \Psi^2 \, dx \, dy \right]^{-1}. \quad (7)$$

Alternatively, the effective background area (a.k.a. *equivalent noise area* or *effective solid angle*) of a PRF is equal to the reciprocal of the product of its sharpness and the square of its volume

$$\beta \equiv \left[ \iint_{-\infty}^{+\infty} (V \tilde{\Psi})^2 \, dx \, dy \right]^{-1} = \frac{1}{V^2 \text{sharpness}}. \quad (8)$$

The effective background area of a normalized Gaussian PRF is  $4\pi S^2$  px<sup>2</sup>, where  $S$  is the standard deviation in pixels (‘px’); a critically sampled normalized Gaussian PRF has an effective background area of  $4\pi \approx 12.57$  px. King (1983) notes that numerical integration of a realistic ground-based stellar profile gives an effective background area of  $30.8S^2$  instead of the value of  $4\pi S^2$  for a normalized Gaussian profile.

### 2.2 Basic least-squares fitting theory

Consider a CCD observation of two overlapping stellar images. Assuming that we already know the PSF and the DRF of the observation, a simple model of the observation will have seven parameters: two stellar intensities<sup>1</sup> ( $\mathcal{E}_1, \mathcal{E}_2$ ) in electrons, four coordinate values,

<sup>1</sup> Stellar intensity is defined to be the total number of electrons from a single star scaled to a PRF volume integral of 1. The *observed* stellar intensity ( $\equiv \mathcal{E}V$ ) is, by definition, always less than or equal to the *measured* stellar intensity ( $\equiv \mathcal{E}$ ).

giving the stellar positions  $(\mathcal{X}_1, \mathcal{Y}_1, \mathcal{X}_2, \mathcal{Y}_2)$  in pixels, and  $\mathcal{B}$ , which is the *observed* background sky level<sup>2</sup> in electrons (which is assumed to be the same for both stars). These observational parameters are not independent for overlapping stars in the presence of photon and CCD readout noise. The conservation of electron flux will require that if  $\mathcal{E}_1$  increases then  $\mathcal{E}_2$  must decrease and vice versa for a given value of  $\mathcal{B}$ . The most accurate photometry possible is obtained when these dependent parameters are fitted simultaneously. Any reasonable model of two overlapping stellar images will be a non-linear function when the positions and intensities are to be determined simultaneously. The technique of non-linear least-squares fitting was developed to provide for the simultaneous determination of dependent or independent parameters of non-linear model functions.

Assume that we have a calibrated CCD observation with  $N$  pixels and that  $z_i$  is the number of electrons in the  $i$ th pixel, which is located at the position of  $(x_i, y_i)$ , and has a measurement error of  $\sigma_i$  electrons. Let  $m(x, y; p_1, \dots, p_M)$  be an observational model of the CCD electron pixel values that has two coordinates  $(x, y)$  and  $M$  parameters. For notational convenience, let the vector  $r_i$  represent the coordinates  $(x_i, y_i)$  of the  $i$ th pixel and the vector  $\mathbf{p}$  represent all the model parameters  $[\mathbf{p} \equiv (p_1, \dots, p_M)]$ . The observational model of the  $i$ th pixel can thus be compactly written as  $m_i \equiv m(\mathbf{r}_i; \mathbf{p})$ .

The measure of the goodness of fit between the data and the model, called chi square, is defined as

$$\chi^2(\mathbf{p}) \equiv \sum_{i=1}^N \frac{1}{\sigma_i^2} (z_i - m_i)^2. \quad (9)$$

The theory of least-squares minimization states that the optimum value of the parameter vector  $\mathbf{p}$  is obtained when  $\chi^2(\mathbf{p})$  is minimized with respect to each parameter simultaneously. If  $\mathbf{p}_0$  is the optimal parameter vector, then  $\chi^2(\mathbf{p}_0)$  is the absolute minimum of the  $M$ -dimensional manifold  $\chi^2(\mathbf{p})$ .

For some small correction parameter vector  $\delta$ , one can approximate  $\chi^2(\mathbf{p} + \delta)$  by its Taylor series expansion as follows:

$$\begin{aligned} \chi^2(\mathbf{p} + \delta) &= \sum_{n=0}^{\infty} \frac{1}{n!} (\delta \cdot \nabla)^n \chi^2(\mathbf{p}) \\ &\approx \chi^2(\mathbf{p}) + \delta \cdot \nabla \chi^2(\mathbf{p}) + \frac{1}{2} \delta \cdot \mathbf{H} \cdot \delta, \end{aligned} \quad (10)$$

where

$$\begin{aligned} [\mathbf{H}]_{jk} &\equiv \frac{\partial^2 \chi^2(\mathbf{p})}{\partial a_j \partial a_k} \\ &\approx \left[ \frac{\partial \chi^2(\mathbf{p})}{\partial a_j} \right] \left[ \frac{\partial \chi^2(\mathbf{p})}{\partial a_k} \right] \end{aligned} \quad (11)$$

is the  $jk$ th element of the  $M \times M$  Hessian matrix  $\mathbf{H}$  of  $\chi^2(\mathbf{p})$  [e.g. Arfken (1970); Press et al. (1986)]. The approximation for the calculation of the Hessian matrix elements is frequently used whenever the computation of the second partial derivative is numerically unstable. If  $\chi^2(\mathbf{p} + \delta)$  is a *local* minimum of  $\chi^2$  manifold, then it can be shown that

$$\mathbf{H} \cdot \delta = -\nabla \chi^2(\mathbf{p}). \quad (12)$$

By solving this equation for the correction vector  $\delta$ , one can determine a better parameter vector  $\mathbf{p}' = \mathbf{p} + \delta$ . When the parameter vector  $(\mathbf{p})$  is redefined to be the better parameter  $(\mathbf{p}')$ , the Hessian

matrix and the gradient of  $\chi^2(\mathbf{p})$  can then be recalculated to determine a new correction vector  $(\delta)$ . This process repeats until the correction vector is sufficiently small – generally when the difference between the solutions is no longer statistically significant. If the fitting process has not failed, then the optimal parameter vector  $(\mathbf{p}_0)$  should be very close to the true parameter vector.

Once the optimal parameter vector has been determined, the covariance matrix  $\mathbf{C}$  may then be calculated by inverting the Hessian matrix  $\mathbf{H}$  computed with the optimal parameter vector. The standard errors (one standard deviation) of the fitted parameters can be estimated as follows:

$$\sigma_j \approx \sqrt{[\mathbf{C}]_{jj}} = \left[ \sum_{i=1}^N \frac{1}{\sigma_i^2} \left( \frac{\partial m_i}{\partial p_j} \right)^2 \right]^{-1/2}, \quad (13)$$

where  $\sigma_j$  is the standard error associated with the  $j$ th parameter  $(p_j)$ . Usage of equation (13) for error estimates is based on the critical assumption that fitted model parameters are independent (indicated by negligibly small off-diagonal elements of the covariance matrix). It is important to note that whenever this critical assumption is violated, the results produced by least-squares fitting may not be statistically reliable, which is to say, they may no longer be physically meaningful.

## 2.3 Photometry

The theoretical photometric performance limits for PSF-fitting CCD stellar photometry can be derived using a simple observational model consisting of a PRF and a constant sky level.

### 2.3.1 Observational model

Consider a CCD observation of a single isolated star on a flat sky background. Assuming that one already knows the PRF of the observation at the location of the star, a simple model of the observation would have just two parameters: the stellar intensity ( $\mathcal{E}$ ) in electrons, and the observed background sky level ( $\mathcal{B}$ ) in electrons. The observational model for the  $i$ th pixel would be

$$m_i \equiv \mathcal{B} + \mathcal{E} V \tilde{\Psi}_i, \quad (14)$$

where  $V$  is the volume integral of the PRF and  $\tilde{\Psi}_i$  is the value of the  $i$ th pixel of the *normalized* PRF ( $\tilde{\Psi}_i \equiv \Psi_i / V$ ).

### 2.3.2 Bright star limit

In the case of bright stars, most of the electrons found in the  $i$ th pixel of the observation will come from the star and not the sky

$$m_i \approx \mathcal{E} V \tilde{\Psi}_i. \quad (15)$$

The actual number of electrons found in the  $i$ th pixel will be described by a Poisson distribution with a mean and variance of  $m_i$ . The measurement error (one standard deviation) for the  $i$ th pixel would thus be

$$\begin{aligned} \sigma_i &= \sqrt{m_i} \\ &\approx \sqrt{\mathcal{E} V \tilde{\Psi}_i}. \end{aligned} \quad (16)$$

All other noise sources (due to, e.g. the observed background sky, instrumental readout noise, flat-field calibrations errors, etc.) are assumed, in this special case, to be negligibly small.

<sup>2</sup> The observed background sky level (in electrons) is the product of true background sky level (in photons) and the *average* PRF volume *across a pixel*:  $\mathcal{B} \equiv \mathcal{B}_{\text{true}}(V)$ .

The variance of the stellar intensity measurement error of bright stars can be estimated using equations (13), (14) and (16) as follows:

$$\begin{aligned}\sigma_{\mathcal{E}: \text{bright}}^2 &\approx \left[ \sum_{i=1}^N \frac{1}{\mathcal{E} V \tilde{\Psi}_i} \left( \frac{\partial}{\partial \mathcal{E}} \mathcal{E} V \tilde{\Psi}_i \right)^2 \right]^{-1} \\ &\approx \frac{\mathcal{E}}{V} \left[ \iint_{-\infty}^{+\infty} \tilde{\Psi} \, dx \, dy \right]^{-1} \\ &= \frac{\mathcal{E}}{V},\end{aligned}\quad (17)$$

as expected from photon statistics.

A bright isolated star with an intensity of  $10^6$  photons imaged with a perfect CCD detector would have a stellar image with  $10^6 \, \text{e}^- (= \mathcal{E})$  and a stellar intensity measurement error of  $\sigma_{\mathcal{E}} \approx \sqrt{\mathcal{E}/(V \equiv 1)} = 10^3 \, \text{e}^-$ . The same star imaged with an inefficient CCD detector with a QE of 25 per cent ( $V = 1/4$ ) would have a stellar image with  $\sim 250\,000 \, \text{e}^-$ , which would have a Poisson noise error of  $\sim 500 \, \text{e}^-$ . The *measured* stellar intensity is  $\mathcal{E} \approx 10^6 \, \text{e}^-$  with an rms measurement error of  $\sigma_{\mathcal{E}} \approx \sqrt{\mathcal{E}/V} = 2000 \, \text{e}^-$ , which is two times larger than it would be with a perfect detector and four times larger than the Poisson noise error of the *observed* number of electrons.

Solving for *measured* stellar intensity ( $\equiv \mathcal{E}$ ) instead of the *observed* stellar intensity ( $\equiv \mathcal{E}V$ ) enables the creation of stellar photometric reduction programs capable of dealing with intrapixel QE variations through the accurate modelling of the image-formation process within the detector. While it is certainly convenient to assume that one's detector has negligible intrapixel QE variation, in the real world even NASA-grade CCD detectors, like those found in the *HST* WFPC2 instrument, can have peak-to-peak intrapixel sensitivity variations greater than 0.02 mag ( $> 2$  per cent) (see figs 5 and 6 of Lauer 1999).

### 2.3.3 Faint star limit

Most of the electrons found in the  $i$ th pixel of an observation of a *faint* isolated star on a flat sky background will come from the sky and not from the star. In that case, the measurement error associated with the  $i$ th pixel is approximately the effective background noise level

$$\sigma_i \approx \sigma_{\text{rms}}, \quad (18)$$

where

$$\sigma_{\text{rms}} \equiv \sqrt{\frac{1}{N} \sum_{i=1}^N \sigma_i^2} \quad (19)$$

$$\approx \sqrt{\mathcal{B} + \sigma_{\text{RON}}^2}, \quad (20)$$

$\mathcal{B}$  is the constant observed background sky level, which is assumed to be a Poisson distribution with a mean of  $\mathcal{B}$  electrons, and  $\sigma_{\text{RON}}$  is the rms readout noise.

The variance of the stellar intensity measurement error of faint stars can be estimated using equations (13), (14), (18)–(20) and (8)

as follows:

$$\begin{aligned}\sigma_{\mathcal{E}: \text{faint}}^2 &\approx \left[ \sum_{i=1}^N \frac{1}{\sigma_{\text{rms}}^2} \left( \frac{\partial}{\partial \mathcal{E}} \mathcal{E} V \tilde{\Psi}_i \right)^2 \right]^{-1} \\ &\approx \frac{\sigma_{\text{rms}}^2}{V^2} \left[ \iint_{-\infty}^{+\infty} \tilde{\Psi}^2 \, dx \, dy \right]^{-1} \\ &= \beta \sigma_{\text{rms}}^2\end{aligned}\quad (21)$$

$$\approx \beta [\mathcal{B} + \sigma_{\text{RON}}^2], \quad (22)$$

where  $\beta$  is the effective background area of the PRF. Equation (22) agrees with equation (9) of King (1983) for a perfect ( $V \equiv 1$ ) noiseless ( $\sigma_{\text{RON}} \equiv 0 \, \text{e}^-$ ) detector.

An important additional noise source for the photometry of faint stars is the systematic error due to the uncertainty of the measurement of the background. If the sky background is assumed to be flat, then the rms measurement error of the constant sky background can be estimated using equations (13), (14), (18)–(20) as follows:

$$\begin{aligned}\sigma_{\mathcal{B}} &\approx \left[ \sum_{i=1}^N \frac{1}{\sigma_{\text{rms}}^2} \left( \frac{\partial}{\partial \mathcal{B}} \mathcal{B} \right)^2 \right]^{-1/2} \\ &= \frac{\sigma_{\text{rms}}}{\sqrt{N}}\end{aligned}\quad (23)$$

$$\approx \sqrt{\frac{\mathcal{B} + \sigma_{\text{RON}}^2}{N}}. \quad (24)$$

Given a CCD observation with no readout noise, equation (24) reduces to the value of  $\sigma_{\mathcal{B}} = \sqrt{\mathcal{B}/N}$  expected from simple sampling statistics.

The portion of the rms stellar intensity measurement error that is caused by the error in the determination of the local sky level is  $\sigma_{\mathcal{B}} \beta$  (Irwin 1985). While this error is frequently negligible for bright stars, it is generally significant for faint stars. Including the uncertainty in the determination of the constant observed background sky level thus gives a more realistic estimate for the rms stellar intensity measurement error for *faint* stars as follows:

$$\begin{aligned}\sigma_{\mathcal{E}: \text{faint}} &\approx \sqrt{\beta \sigma_{\text{rms}}^2} + \beta \sigma_{\mathcal{B}} \\ &= \sqrt{\beta} \left( 1 + \sqrt{\beta/N} \right) \sigma_{\text{rms}}\end{aligned}\quad (25)$$

$$\approx \sqrt{\beta} \left( 1 + \sqrt{\beta/N} \right) \sqrt{\mathcal{B} + \sigma_{\text{RON}}^2}. \quad (26)$$

Precise and accurate stellar photometry of faint stars requires an excellent determination of the observed background sky which, in turn requires accurate background sky models. Given a valid background sky model, small apertures will be more sensitive to background sky measurement errors than large apertures.

### 2.3.4 Photometric performance model

A realistic photometric performance model for CCD PSF-fitting photometry can be created by combining the bright and faint star limits developed above. The theoretical *upper limit* for the photometric signal-to-noise ratio (S/N) of CCD PSF-fitting photometric

algorithms is as follows:

$$\begin{aligned} S/N &\equiv \frac{\mathcal{E}}{\sigma_{\mathcal{E}}} \\ &\approx \frac{\mathcal{E}}{\sqrt{\sigma_{\mathcal{E}: \text{bright}}^2 + \sigma_{\mathcal{E}: \text{faint}}^2}} \\ &\approx \frac{\mathcal{E}}{\sqrt{\frac{\mathcal{E}}{V} + \beta \left(1 + \sqrt{\beta/N}\right)^2 \sigma_{\text{rms}}^2}} \end{aligned} \quad (27)$$

$$\approx \frac{\mathcal{E}}{\sqrt{\frac{\mathcal{E}}{V} + \beta \left(1 + \sqrt{\beta/N}\right)^2 [\mathcal{B} + \sigma_{\text{RON}}^2]}}. \quad (28)$$

These approximations assume, for the sake of simplicity, that any noise contribution due to dark current and quantization noise is negligible. While these additional noise sources can be added to create an even more realistic performance model for stellar photometry, the assumption of low dark current and minimal quantization noise is realistic for state-of-the-art astronomical-grade CCD imagers. The resulting photometric error is approximately

$$\Delta \text{mag} \approx \frac{1.0857}{S/N}, \quad (29)$$

where the constant 1.0857 is an approximation for Pogson's ratio  $a \equiv 5/\ln(100) = 2.5 \log(e)$  (Pogson 1856).

### 2.3.5 Cramér–Rao lower bound

The Cramér–Rao lower bound (CRLB) is the lower bound on the variance of *any* unbiased estimator. Since it is physically impossible to find an unbiased estimator that beats the CRLB, the CRLB provides a performance benchmark against which any unbiased estimator can be compared.

The CRLB for stellar photometry of a single isolated star imaged by a two-dimensional photon-counting detector has been derived several times in the astrophysical literature (see, e.g. appendix A of Perryman et al. 1989; Irwin 1985; King 1983). The generalization for a crowded field with overlapping stellar images is given in Jakobsen, Greenfield & Jedrzejewski (1992).

The CRLB for the bright star limit of stellar photometry of a single isolated star is

$$\sigma_{\mathcal{E}: \text{bright-CRLB}}^2 = \mathcal{E}, \quad (30)$$

which is equation (17) with a perfect detector. The CRLB for the faint star limit of stellar photometry of a single isolated star is

$$\sigma_{\mathcal{E}: \text{faint-CRLB}}^2 = \beta \mathcal{B}, \quad (31)$$

which is equation (26) with a noiseless detector and a negligible background measurement error ( $N \rightarrow \infty$ ).

The photometric performance model has bright and faint star limits, which are the same, respectively, as the bright and faint star CRLBs for stellar photometry of a single isolated star on a flat sky background imaged with a perfect noiseless detector.

## 2.4 Astrometry

The theoretical astrometric limits for PSF-fitting CCD stellar photometry can be derived using a simple observational model consisting of a Gaussian PRF and a constant sky level.

### 2.4.1 Observational model

Consider a CCD observation of a single isolated star on a flat sky background. A Gaussian is a good model for the PSF of a ground-based CCD observation since the central core of a ground-based stellar profile is approximately Gaussian (King 1971). In this case the PSF would have three parameters: two coordinate values giving the location  $(\mathcal{X}, \mathcal{Y})$  of the star on the CCD and the standard deviation of the Gaussian ( $\mathcal{S}$ ) in pixels [see equation (5)].

An *imperfect but uniformly flat* DRF ( $V < 1$ ) gives a value for the  $i$ th pixel of the PRF located at  $(x_i, y_i)$ , which is equal to the product of the volume of the PRF and the value of the volume integral of the PSF over the area of the  $i$ th pixel

$$G_i \equiv V \int_{x_i-0.5}^{x_i+0.5} \int_{y_i-0.5}^{y_i+0.5} g(x, y; \mathcal{X}, \mathcal{Y}, \mathcal{S}) dx dy. \quad (32)$$

The actual limits of the above volume integral reflect the appropriate mapping transformation of the  $x$  and  $y$  coordinates onto the CCD pixel coordinate system.

If the PRF has been *oversampled*, the value of the  $i$ th pixel of the PRF is approximately equal to the product of the volume of the PRF and the value of the PSF at the *center of the  $i$ th pixel*

$$G_i \approx V g_i, \quad (33)$$

where

$$g_i \equiv g(x_i, y_i; \mathcal{X}, \mathcal{Y}, \mathcal{S}). \quad (34)$$

A simple model of the observation will require two additional parameters: the stellar intensity ( $\mathcal{E}$ ) and the observed background sky level ( $\mathcal{B}$ ) in electrons. The  $i$ th pixel of the observational model would be

$$m_i \equiv \mathcal{B} + \mathcal{E} V \tilde{G}_i, \quad (35)$$

where  $V$  is the volume integral of the PRF and  $\tilde{G}_i$  is the value of the  $i$ th pixel of the *normalized* PRF ( $\tilde{G}_i \equiv G_i/V \approx g_i$ ).

### 2.4.2 Bright star limit

In the case of bright stars, most of the electrons found in the  $i$ th pixel of the observation will come from the star and not the sky

$$m_i \approx \mathcal{E} V \tilde{G}_i. \quad (36)$$

The actual number of electrons found in the  $i$ th pixel will be described by a Poisson distribution with a mean and variance of  $m_i$ . The measurement error (one standard deviation) for the  $i$ th pixel would thus be

$$\begin{aligned} \sigma_i &= \sqrt{m_i} \\ &\approx \sqrt{\mathcal{E} V \tilde{G}_i}. \end{aligned} \quad (37)$$

All other noise sources (e.g. the observed background sky, instrumental readout noise, flat-field calibrations errors, etc.) are assumed to be negligibly small.

The variance of the stellar  $\mathcal{X}$  position measurement error of a bright isolated *oversampled* star can be estimated using

equations (13), (35), (37), and (5) as follows:

$$\begin{aligned}\sigma_{\mathcal{X}:\text{bright}}^2 &\approx \left[ \sum_{i=1}^N \frac{1}{\mathcal{E}V\tilde{G}_i} \left( \frac{\partial}{\partial \mathcal{X}} \mathcal{E}V\tilde{G}_i \right)^2 \right]^{-1} \\ &\approx \frac{1}{\mathcal{E}V} \left[ \sum_{i=1}^N \frac{1}{g_i} \left( \frac{\partial}{\partial \mathcal{X}} g_i \right)^2 \right]^{-1} \\ &\approx \frac{\mathcal{S}^4}{\mathcal{E}V} \left[ \iint_{-\infty}^{+\infty} g(x, y; \mathcal{X}, \mathcal{Y}, \mathcal{S}) (x - \mathcal{X})^2 dx dy \right]^{-1} \\ &= \frac{\mathcal{S}^2}{\mathcal{E}V} \\ &\approx \frac{\mathcal{L}^2}{\mathcal{E}V},\end{aligned}\quad (38)$$

where

$$\mathcal{L} \equiv \sqrt{\frac{\beta V^2}{4\pi}} = \frac{1}{\sqrt{4\pi \text{sharpness}}} \quad (39)$$

is the *critical-sampling scalelength* of the PRF<sup>3</sup> in pixel units (px), which, unlike  $\mathcal{S}$ , is defined for all PRFs. By definition, the critical-sampling scalelength of a critically sampled PRF imaged with a perfect detector is 1 px.  $\mathcal{L} > 1$  indicates that the PRF is *oversampled*, while  $\mathcal{L} < 1$  indicates that the PRF is *undersampled*.

In the special case of a critically sampled bright star imaged with a perfect detector, one finds that the astrometric performance limit (in pixel units) is equal to the reciprocal of photometric error performance limit

$$\sigma_{\mathcal{X}:\text{bright}} \approx \frac{1}{\sqrt{\mathcal{E}}} \approx \frac{1}{\sigma_{\mathcal{E}:\text{bright}}}.$$

#### 2.4.3 Faint star limit

Let us again assume that the noise contribution from the star is negligibly small and that the variance of the measurement error of the  $i$ th pixel can be replaced with an average constant rms value. The variance of the stellar  $\mathcal{X}$  position measurement error of a faint isolated *oversampled* star can be estimated using equations (13), (35), (18)–(20), and (5) as follows:

$$\begin{aligned}\sigma_{\mathcal{X}:\text{faint}}^2 &\approx \left[ \sum_{i=1}^N \frac{1}{\sigma_{\text{rms}}^2} \left( \frac{\partial}{\partial \mathcal{X}} \mathcal{E}V\tilde{G}_i \right)^2 \right]^{-1} \\ &\approx \frac{\sigma_{\text{rms}}^2}{\mathcal{E}^2 V^2} \left[ \sum_{i=1}^N \left( \frac{\partial}{\partial \mathcal{X}} g_i \right)^2 \right]^{-1} \\ &\approx \frac{\sigma_{\text{rms}}^2 \mathcal{S}^4}{\mathcal{E}^2 V^2} \left[ \iint_{-\infty}^{+\infty} g^2(x, y; \mathcal{X}, \mathcal{Y}, \mathcal{S}) (x - \mathcal{X})^2 dx dy \right]^{-1} \\ &= 8\pi \sigma_{\text{rms}}^2 \frac{\mathcal{S}^4}{\mathcal{E}^2 V^2} \\ &\approx 8\pi \sigma_{\text{rms}}^2 \left( \frac{\mathcal{L}^2}{\mathcal{E}V} \right)^2 \\ &\approx 8\pi \sigma_{\text{rms}}^2 (\sigma_{\mathcal{X}:\text{bright}}^2)^2\end{aligned}\quad (40)$$

<sup>3</sup> From the definition of the effective background area of an oversampled Gaussian PRF with  $V < 1$ ,  $\beta_G \equiv 4\pi\mathcal{S}^2/V^2$ , one sees that critical-sampling scalelength has been designed to be a proxy for any PRF.

$$\approx 8\pi (\mathcal{B} + \sigma_{\text{RON}}^2) (\sigma_{\mathcal{X}:\text{bright}}^2)^2. \quad (41)$$

#### 2.4.4 Astrometric performance model

A realistic performance model for CCD PSF-fitting astrometry can be created by combining the bright and faint star limits developed above. The expected *lower limit* of the rms measurement error for the stellar  $\mathcal{X}$  position for a single isolated star on a flat sky can be estimated as follows:

$$\begin{aligned}\sigma_{\mathcal{X}} &\approx \sqrt{\sigma_{\mathcal{X}:\text{bright}}^2 + \sigma_{\mathcal{X}:\text{faint}}^2} \\ &\approx \sqrt{\frac{\mathcal{L}^2}{\mathcal{E}V} \left[ 1 + 8\pi \sigma_{\text{rms}}^2 \frac{\mathcal{L}^2}{\mathcal{E}V} \right]}\end{aligned}\quad (42)$$

$$\approx \sqrt{\frac{\mathcal{L}^2}{\mathcal{E}V} \left[ 1 + 8\pi (\mathcal{B} + \sigma_{\text{RON}}^2) \frac{\mathcal{L}^2}{\mathcal{E}V} \right]}. \quad (43)$$

The rms stellar  $\mathcal{Y}$  position measurement error is, by symmetry, the same as for  $\mathcal{X}$

$$\sigma_{\mathcal{Y}} = \sigma_{\mathcal{X}}. \quad (44)$$

#### 2.4.5 Photonic limit and the Cramér–Rao lower bound

The CRLB for stellar astrometry depends not only on the signal-to-noise ratio, but also on the *size* and *shape* of the detector. For well-sampled data, the size and shape of the detector can be ignored and a CRLB can be found for a perfect noiseless detector with infinitely small pixels. This is called the *photonic limit*.

The determination of the CRLB for astrometry becomes much more complicated with *undersampled* observations. Astrometric precision degrades when the size of the detector is comparable to the size of the stellar image – the quality of the position estimation is then dependent on the fraction of photons falling *outside* of the central pixel. The worst-case scenario for stellar astrometry occurs when *all* the light from a star falls within a single pixel: all one knows for sure, in that unfortunate case, is that the star is located *somewhere* within the central (and only) pixel.

The photonic limit (PL) for stellar astrometry of a bright well-sampled single isolated normalized Gaussian star is

$$\begin{aligned}\sigma_{\mathcal{X}:\text{bright-PL}}^2 &= \frac{\mathcal{S}^2}{\mathcal{E}} \\ (\text{Irwin 1985}). \text{ Using } \mathcal{L} \text{ as a proxy for } \mathcal{S}, \text{ one has the generalized form for any PSF:} \\ \sigma_{\mathcal{X}:\text{bright-PL}}^2 &\approx \frac{\mathcal{L}^2}{\mathcal{E}},\end{aligned}\quad (45)$$

which is equation (38) with a perfect detector.

The photonic limit for stellar astrometry of a faint well-sampled single isolated normalized Gaussian star is (Irwin 1985)

$$\sigma_{\mathcal{X}:\text{faint-PL}}^2 = \frac{8\pi \mathcal{B} \mathcal{S}^4}{\mathcal{E}^2}.$$

Using  $\mathcal{L}$  as a proxy for  $\mathcal{S}$ , one has the generalized form for any PSF

$$\sigma_{\mathcal{X}:\text{faint-PL}}^2 \approx \frac{8\pi \mathcal{B} \mathcal{L}^4}{\mathcal{E}^2}, \quad (46)$$

which is equation (41) with a perfect noiseless detector.



The astrometric performance model has bright and faint star limits that are the same, respectively, as the bright and faint star photonic astrometric limits, which are the CRLBs for stellar astrometry of a single isolated Gaussian star on a flat sky background imaged with a perfect noiseless detector with infinitely small pixels. The CRLBs for stellar astrometry of a single isolated Gaussian star on a flat sky background imaged with a perfect noiseless CCD with square pixels (Winick 1986) quickly approaches the photonic limits with *well-sampled* observations; undersampled observations will have larger astrometric errors than predicted by the photonic limits.

## 2.5 Relation between astrometric and photometric errors

### 2.5.1 Bright star limit

Following King (1983) and Irwin (1985), we can now compare the astrometric error of bright isolated stars with their photometric error. The ratio of the astrometric error of a bright isolated star and the critical-sampling scalelength of the PRF is equal to the ratio of the stellar intensity measurement error and the stellar intensity

$$\frac{\sigma_{\mathcal{X}}}{\mathcal{L}} = \frac{\sigma_{\mathcal{E}}}{\mathcal{E}}. \quad (47)$$

For example, a bright isolated critically sampled star with one million electrons imaged on a perfect detector ( $\mathcal{E} = 10^6 \text{ e}^-$ ,  $V \equiv 1$  and  $\mathcal{L} = 1 \text{ px}$ ) would, theoretically, have a signal-to-noise ratio of  $S/N = 1000$ , a stellar intensity measurement error of  $\sigma_{\mathcal{E}} = 1000 \text{ e}^-$  and an rms position error in  $x$  of one-thousandth of a pixel ( $\sigma_{\mathcal{X}} = 0.001 \text{ px}$ ). Such astrometric accuracy may be difficult to achieve in practice under normal ground-based observing conditions even with state-of-the-art astronomical-grade CCD cameras.

### 2.5.2 Faint star limit

The astrometric error of faint isolated stars is related to their photometric error as follows:

$$\frac{\sigma_{\mathcal{X}}}{\mathcal{L}} \approx \left( \frac{\sigma_{\mathcal{E}}}{\mathcal{E}} \right) \frac{\sqrt{2}}{1 + \sqrt{\beta/N}}. \quad (48)$$

For example, a faint isolated critically sampled star imaged with a perfect detector with a 20 per cent intensity measurement error and a negligible background measurement error ( $N \rightarrow \infty$ ) would, theoretically, have an astrometric error of  $\sim 0.283 [\approx (0.200 \sqrt{2})] \text{ px}$ .

### 2.5.3 Practical lower bound

These results suggest the following practical lower bound for astrometric errors with respect to photometric errors:

$X$  per cent photometry gives no better than  $X$  per cent astrometry with respect to the critical-sampling scalelength ( $\mathcal{L}$ ).

For example, a star with 1 per cent stellar photometry will have no better than 1 per cent astrometry with respect to the critical-sampling scalelength. If the star is critically sampled, then the astrometric precision will be no better than 0.01 px.

All of the above derivations are based on the assumption that that flat-field calibration errors are negligible. The relation between photometry and astrometry for bright isolated stars can fail with large flat-field calibration errors.

## 3 DISCRETE POINT SPREAD FUNCTIONS

A *discrete* PSF is a sampled version of a continuous two-dimensional PSF. The shape information about the photon scattering pattern of a discrete PSF is typically encoded using a numerical table (matrix). An *analytical* PSF has the shape information encoded with continuous two-dimensional mathematical functions.

In order to do accurate stellar photometry and astrometry with discrete PSFs one needs to be able to (i) accurately shift discrete PSFs to new positions within the observational model, and (ii) compute the position-partial derivatives of discrete PSFs. The next two subsections describe how these tasks may be accomplished using numerical analysis techniques.

### 3.1 Moving discrete PSFs

Building a realistic observation model requires the placement of a star at the desired location within the model; this is done by determining the PRF at the required location, and then multiplying it by the stellar intensity. With PSFs encoded by mathematical functions, one just computes the PSF at the desired location in the observational model. With discrete PSFs, one ideally takes a reference PSF (typically derived/computed for the center of a pixel) and shifts it to the desired location using a perfect two-dimensional interpolation function. But, how is this done in practice? The sinc function,  $\sin(\pi x)/(\pi x)$ , is, theoretically, a perfect two-dimensional interpolation function. Unfortunately, the sinc function decays with  $1/x$  and never actually reaches zero. One can use a windowed interpolant in order to improve computational speed – but one must be cautious about aliasing effects caused by using a windowed function. In the case of stellar photometry and astrometry, aliasing effects will generally only be seen with bright stars since a large number of photons are required to adequately sample the higher spatial frequencies of the PSF.

The following 21-px-wide *damped sinc function* interpolant does an excellent job interpolating discrete PSF (Mighell 2002) :

$$f^{\text{shifted}}(x_0) \equiv \sum_{i=-10}^{10} f(x_i) \frac{\sin(\pi(x_i - x_0))}{\pi(x_i - x_0)} \exp \left[ - \left( \frac{x_i - x_0}{3.25} \right)^2 \right]. \quad (49)$$

Note that since the two-dimensional sinc function is separable in  $x$  and  $y$ , this interpolant can be coded to be computationally fast and efficient. This interpolant, from the ZODIAC C library written by Marc Buie of Lowell Observatory, was specifically designed for use with 32-bit floating numbers.

Aliasing problems due to critically sampled or undersampled data may be overcome by using discrete PSFs that are *supersampled* at two, three or more times more finely than the observational data. In order to have a realistic observational model, once the supersampled discrete PSF has been interpolated to the correct position, a new *degraded* (rebinned) version of the discrete PSF must be created that has the same spatial resolution as the observational data.

### 3.2 Position-partial derivatives of discrete PSFs

While the mathematics of determining the position-partial derivatives of individual stars within the observational model with respect to the  $x$  and  $y$  direction vectors is the same regardless of how the shape information in a PSF is encoded, the implementation methodology for the computation of position-partial derivatives of discrete PSFs is very different than the one used for analytical PSFs.

The position-partial derivatives of discrete PSFs can be determined using *numerical differentiation techniques* on the discrete PSF.

It is a standard practice in numerical analysis to approximate the first, second or higher, derivatives of a tabulated function  $f(x_i)$  with multipoint formulae. Abramowitz & Stegun (1964) give 18 different multipoint formulae, which can be used (with varying degrees of accuracy) to approximate the first derivative of the tabulated function  $f(x_i)$ . The following five-point differentiation formula (Abramowitz & Stegun 1964, p. 914),

$$f'(x_i) \approx \frac{1}{12} [f(x_{i-2}) - 8f(x_{i-1}) + 8f(x_{i+1}) - f(x_{i+2})], \quad (50)$$

works well with discrete PSFs (Mighell 2002). This approximation takes just four additions and three multiplications, which generally makes it considerably faster to compute than the traditional determination of the partial derivative of the volume integral of the PSF above a CCD pixel.

#### 4 THE MATPHOT ALGORITHM

The concepts presented above outline the unique and fundamental features of the MATPHOT algorithm for accurate and precise stellar photometry using discrete PSFs.

While the key features of a CCD stellar photometric reduction algorithm can be described in an article, the full implementation of such an algorithm generally exists as a complex computer program consisting of many thousands of lines of computer code. Since good algorithms can be poorly implemented, it can be difficult to differentiate between a poor algorithm and a poorly coded implementation of a good algorithm.

Confidence in a complex algorithm can be established by developing an implementation of the algorithm that meets theoretical performance expectations. The following subsection describes a real-world implementation of the MATPHOT algorithm that meets the theoretical performance expectations for accurate and precise stellar photometry and astrometry, which are derived in Section 2.

##### 4.1 MPD: MATPHOT Demonstrator

I have written a C-language computer program, called MPD,<sup>4</sup> which is based on the current implementation of the MATPHOT algorithm for precise and accurate stellar photometry using discrete PSFs. The MPD code demonstrates the precision and accuracy of the MATPHOT algorithm by analysing simulated CCD observations based on user-provided discrete PSFs encoded as FITS (Flexible Image Transport System) images (Wells, Greisen & Harten 1981). Discrete PSFs are shifted within the observational model using the 21-pixel-wide damped sinc interpolation function given in equation (49). Position-partial derivatives of discrete PSFs are computed using the five-point differentiation formula given in equation (50). Accurate and precise stellar photometry and astrometry of *undersampled* CCD observations can be obtained with the MPD code when it is presented with *supersampled* discrete PSFs that are sampled two, three or more times more finely than the observational data. The

MPD code is based on a robust implementation of the Levenberg–Marquardt method of non-linear least-squares minimization (Levenberg 1944; Marquardt 1963, also Mighell 1989). When presented with simulated observations based on a Gaussian PSF with a known FWHM (full width at half maximum) value,<sup>5</sup> the MPD code can analyse the observation in two different ways: (i) the MATPHOT algorithm can be used with a discrete Gaussian PSF, or (ii) analytical techniques (Mighell 1989, 1999) can be used with an analytical Gaussian PSF.

## 5 SIMULATED OBSERVATIONS

### 5.1 Oversampled PSFs

I now demonstrate that the theoretical performance limits of Section 2 provide practical performance metrics for photometry and astrometry of CCD stellar observations that are analysed with oversampled Gaussian PSFs.

#### 5.1.1 Analytical PSFs

20 000 *oversampled* CCD stellar observations were simulated and analysed using the MPD code. The CCD detector was assumed to be perfect ( $V \equiv 1$ ) with a CCD readout noise value of  $\sigma_{\text{RON}} = 3 \text{ e}^- \text{ px}^{-1}$ . Stars were simulated using an *analytical* Gaussian PSF with a FWHM  $\equiv 3 \text{ px}$  located near the center of  $60 \times 60 \text{ px}$ , the input stellar intensities ranged from  $-6$  to  $-15 \text{ mag}^6$  ( $251 \leq \mathcal{E}_{\text{true}} \leq 10^6 \text{ e}^-$ ), and a flat background was assumed with a value of  $\mathcal{B} = 100 \text{ e}^-$ . Photon and readout noise were simulated, respectively, using Poisson and Gaussian random noise generators, and the resulting observed background sky measurement error was  $\sigma_{\mathcal{B}} = 0.18 \text{ e}^-$ . The median effective background area of the PRF of these observations was  $\beta = 21.44 \text{ px}^2$ . All the simulated observations were analysed with MPD using an *analytical* Gaussian PSF with FWHM  $\equiv 3.0 \text{ px}$ .

The binned absolute photometric errors are shown as black box-and-whiskers plots (see Appendix A) in the top panel of Fig. 1. The absolute photometric error of an observation is the absolute value of the difference between the measured (estimated) and true (actual) stellar magnitude:  $\Delta \text{mag} \equiv |\text{mag} - \text{mag}_{\text{true}}|$ . The four grey limits seen in the top panel of Fig. 1 are theoretical predictions (derived from Section 2.3.4) for the median (50 per cent cumulative fraction: grey solid curve), top hinge (75 per cent: bottom of the grey band), top fence ( $\sim 98.35$  per cent: top of band), and  $5\sigma$  outlier ( $\sim 99.99997$  per cent: grey dashed curve) values. If the rms photometric error is called  $\sigma_{\text{mag}}$ , then the values of these theoretical limits are approximately equal to  $0.674 \sigma_{\text{mag}}$ ,  $1.151 \sigma_{\text{mag}}$ ,  $2.398 \sigma_{\text{mag}}$  and  $5.423 \sigma_{\text{mag}}$ , respectively. If the photometric performance model is correct and MPD has been coded correctly, then (i) the observed median values (central bar in each box) should intersect the theoretical median value, (ii) most of the top whiskers should be found inside the band and (iii) most of the outliers should be found above the top of the band and all of the outliers should found below the  $5\sigma$  outlier limit.

Comparing the absolute photometric errors of the 20 000 simulated CCD observations with the grey theoretical limits, one sees that the photometric performance of the MPD code is very well predicted by the model given in Section 2.3.4

<sup>4</sup> All source code and documentation for MPD and support software are freely available at the official MATPHOT website at NOAO: <http://www.noao.edu/staff/mighell/matphot>

<sup>5</sup> The FWHM value of a Gaussian is equal to  $2\sqrt{\ln(4)}$  times the standard deviation,  $\mathcal{S}$ , of the Gaussian:  $\text{FWHM} \approx 2.35482 \mathcal{S}$  (see equation 5).

<sup>6</sup> The MATPHOT magnitude system assumes that  $0 \text{ mag} \equiv 1 \text{ e}^-$  (electron)  $\equiv 1 \gamma$  (photon) for a PRF volume of one ( $V = 1$ ).

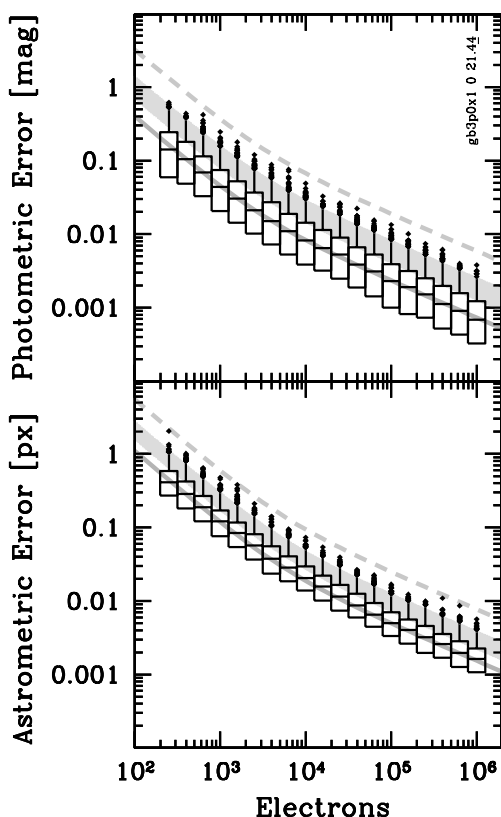


**Figure 1.** The absolute photometric errors (top) and total astrometric errors (bottom) of 20 000 simulated CCD stellar observations analysed with MPD using an oversampled *analytical* Gaussian PSF with a FWHM of 3.0 px ( $\beta \approx 21.44$  px<sup>2</sup>;  $V \equiv 1$ ).

The binned total astrometric errors are shown as black box-and-whiskers plots in the bottom panel of Fig. 1. The total astrometric error of an observation is the distance between the measured (estimated) and true (actual) position of a star:  $\Delta r \equiv \sqrt{(\mathcal{X} - \mathcal{X}_{\text{true}})^2 + (\mathcal{Y} - \mathcal{Y}_{\text{true}})^2}$ . The four grey limits seen in the bottom panel of Fig. 1 are theoretical predictions (derived from Section 2.4.4) for the median (50 per cent cumulative fraction: grey solid curve), top hinge (75 per cent: bottom of the grey band), top fence ( $\sim 98.97$  per cent: top of band), and  $5\sigma$  outlier (99.9997 per cent: grey dashed curve) values. The values of these theoretical limits are approximately equal to  $1.178 \sigma_{\mathcal{X}}$ ,  $1.666 \sigma_{\mathcal{X}}$ ,  $3.027 \sigma_{\mathcal{X}}$  and  $5.890 \sigma_{\mathcal{X}}$ , where  $\sigma_{\mathcal{X}}$  is the rms measurement error for the stellar  $\mathcal{X}$  position. If the astrometric performance model is correct and MPD has been coded correctly, then (i) the observed median values should intersect the theoretical median value, (ii) most of the top whiskers should be found inside the band and (iii) most of the outliers should be found above the top of the band and all of the outliers should be found below the  $5\sigma$  outlier limit.

Comparing the total astrometric errors of the 20 000 simulated CCD observations with the grey theoretical limits, one sees that the astrometric performance of the MPD code is very well predicted by the model given in Section 2.4.4

Fig. 2 shows the *relative* stellar intensity errors and the *relative*  $\mathcal{X}$  position errors of the 20 000 stars analysed in Fig. 1. The relative stellar intensity error is the difference between the measured (estimated) and true (actual) stellar intensity values divided by the estimated stellar intensity error:  $\Delta \mathcal{E} \equiv (\mathcal{E} - \mathcal{E}_{\text{true}})/\sigma_{\mathcal{E}}$ . The relative  $\mathcal{X}$  position error is the difference between the measured (estimated)

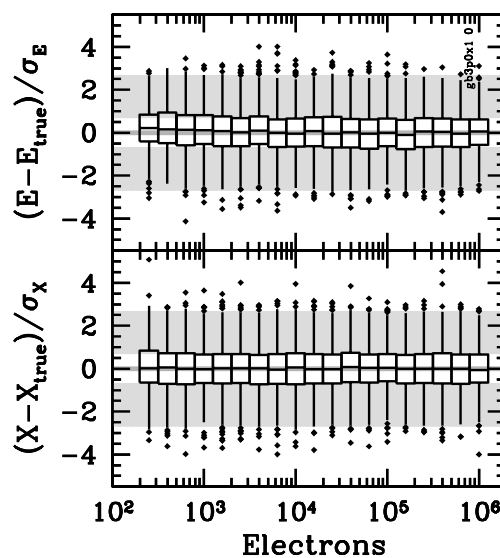


**Figure 2.** Relative stellar intensity errors (top) and relative  $\mathcal{X}$  position errors (bottom) of the data set used in Fig. 1.

and true (actual) stellar  $\mathcal{X}$  position values divided by the estimated  $\mathcal{X}$  error:  $\Delta \mathcal{X} \equiv (\mathcal{X} - \mathcal{X}_{\text{true}})/\sigma_{\mathcal{X}}$ . If MPD has been coded correctly, the relative error distributions for the stellar parameters  $\mathcal{E}$ ,  $\mathcal{X}$  and  $\mathcal{Y}$  should be *normally* distributed. The five grey limits seen in each panel are theoretical predictions (based on the normal distribution) for, from bottom to top, the bottom fence ( $\sim 0.35$  per cent cumulative fraction: bottom of the bottom grey band), bottom hinge (25 per cent: top of bottom band), median (50 per cent: grey solid line at zero), top hinge (75 per cent: bottom of top band), top fence ( $\sim 99.65$  per cent: top of top band) values. If the relative errors for  $\mathcal{E}$  and  $\mathcal{X}$  are indeed normally distributed, then (i) the observed median values should be near zero, (ii) most of the whiskers should be found inside the bands, and (iii) most of the outliers should be beyond the fence values.

Comparing the relative errors for  $\mathcal{E}$  and  $\mathcal{X}$  of the 20 000 simulated CCD observations with the grey theoretical limits, one sees that these errors are, as expected, normally distributed.

The MPD code works well with oversampled analytical Gaussian PSFs and its performance can be very well predicted with the photometric and astrometric models derived in Section 2.

### 5.1.2 Discrete PSFs

The 20 000 simulated CCD observations analysed in Figs 1 and 2 were *reanalysed* with MPD using an oversampled *discrete* Gaussian PSF with a FWHM of 3 px. Fig. 3 shows the resultant absolute photometric errors and total astrometric errors. Fig. 4 shows the resultant relative errors for  $\mathcal{E}$  and  $\mathcal{X}$ . Note how similar Figs 1 and 3 and Figs 2 and 4 are to each other.

Despite the very different way the shape information of the PSF was encoded (i.e. *discrete* versus *analytical* representations), MPD produced nearly identical photometric and astrometric results.

How similar are the measured stellar positions? Fig. 5 shows the *relative*  $\mathcal{X}$  and  $\mathcal{Y}$  position *differences* between the previous analytical and numerical analyses with the MPD code. The top panel shows the difference between the numerical  $\mathcal{X}$  result and the analytical  $\mathcal{X}$  result divided by the estimated error of the analytical result. Similarly, the bottom panel shows the difference between the numerical  $\mathcal{Y}$  result and the analytical  $\mathcal{Y}$  result divided by the estimated error

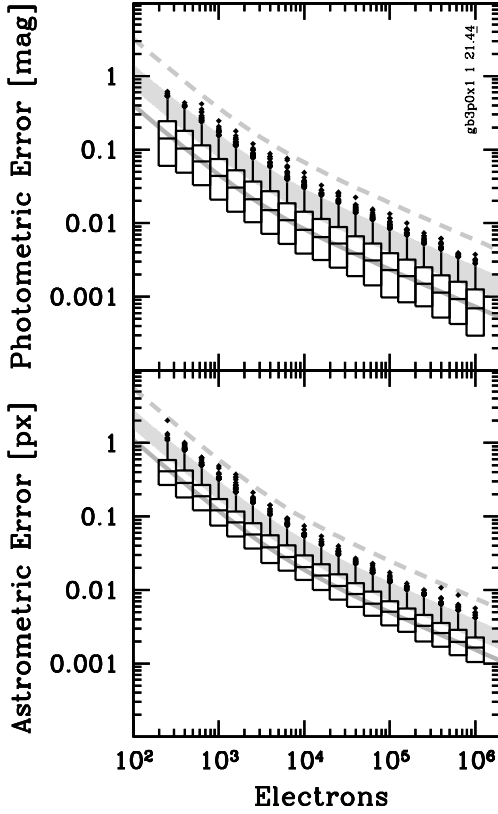


**Figure 3.** The absolute photometric errors (top) and total astrometric errors (bottom) of 20 000 simulated CCD stellar observations used in Figs 1 and 2 were analysed with MPD using an oversampled *discrete* Gaussian PSF with a FWHM of 3.0 px ( $\beta \approx 21.44$  px<sup>2</sup>;  $V \equiv 1$ ).

of the analytical result. The relative differences between the numerical and analytical methods are *not* normally distributed – observe how much smaller the values on the ordinate of Fig. 5 are compared to those of Figs 2 and 4. Figs 2 and 4 *are* normally distributed, and the source of the scatter is photon noise. Fig. 5 indicates that the relative differences between the numerical and analytical methods for astrometry are less than one-fifteenth of the difference due to photon noise. In other words, the computational noise due to the chosen analysis method (numerical versus analytical) is insignificant when compared to the unavoidable photon noise due to the random arrival of photons in any astronomical CCD observation.

The MPD code works as well with oversampled discrete Gaussian PSFs as it does with oversampled analytical Gaussian PSFs.

### 5.1.3 Inefficient detectors

While the volume,  $V$ , of the PRF was carefully tracked throughout the derivation of the photometric and astrometric performance models in Section 2, all previous simulations have assumed a perfect detector ( $V \equiv 1$ ). Let us now check to see if the effects of a PRF volume integral that is less than 1 has been correctly accounted for in the performance models of Section 2 by analysing simulated observations imaged on a very inefficient detector ( $V \ll 1$ ).

20 000 oversampled CCD stellar observations were simulated assuming a very inefficient detector with  $V = 1/9$ . Stars were simulated using a discrete Gaussian PSF with a FWHM  $\equiv 3$  px located near the center of  $60 \times 60$  px, the input stellar intensities ranged from  $-8$  to  $-15$  mag ( $1585$  to  $10^6$   $\gamma$ ); and the

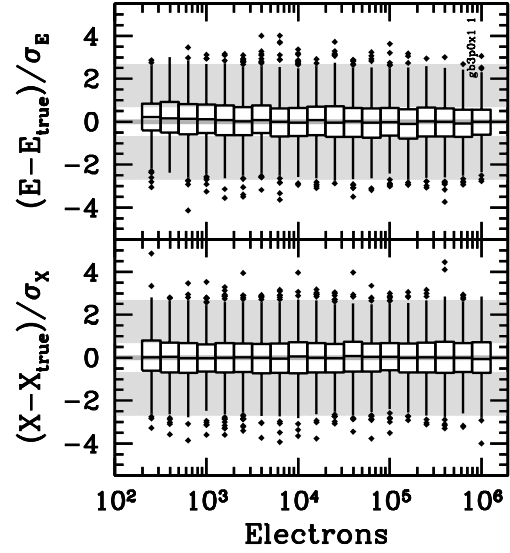


**Figure 4.** Relative stellar intensity errors (top) and relative  $X$  position errors (bottom) of the data set used in Fig. 3.

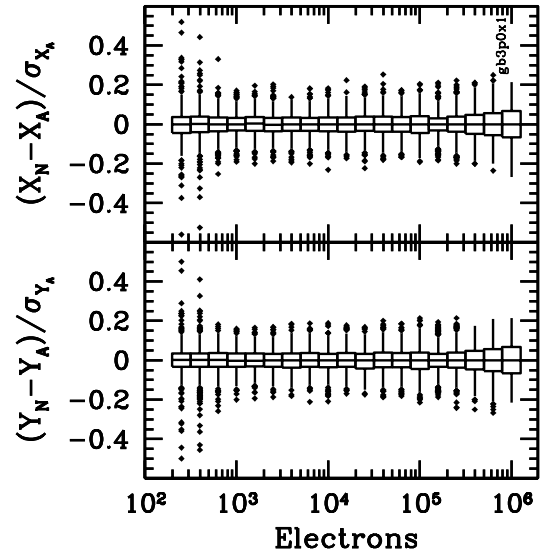


**Figure 5.** Relative  $X$  and  $Y$  position differences (top and bottom, respectively) between the numerical (*subscript N*) and analytical (*subscript A*) results of the same 20 000 stars used in Figs 1–4.

*observed* background sky level was assumed to be a constant value of  $\mathcal{B} = 11.1111$  e<sup>−</sup> ( $\mathcal{B}_{\text{true}} = 100\gamma$ ,  $\langle V \rangle = 1/9$ ), all other simulation parameters were the same as before.

All the simulated observations were analysed with MPD in the same way as described for the numerical experiment shown in Fig. 3 – except that the volume of the PRF was set to  $V = 1/9$  in order to simulate the use of an inefficient detector that converts only  $\sim 11.1$  per cent of photons to electrons.

Fig. 6 shows the absolute photometric errors and total astrometric errors of this numerical experiment. The median effective background area of PRF of these observations was  $\beta \approx 1736.79$  px<sup>2</sup>, which is, as expected,  $81 (= V^{-2})$  times larger than the median value reported in Fig. 3.

Comparing the simulation results with the grey theoretical limits, one sees that the photometric and astrometric performance of

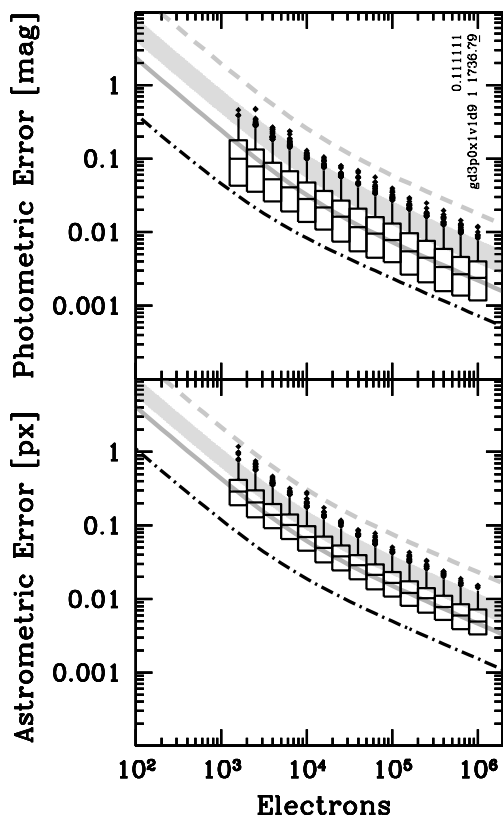


**Figure 6.** The absolute photometric errors (top) and total astrometric errors (bottom) of 20 000 simulated CCD stellar observations analysed with MPD using a discrete Gaussian PSF with a FWHM of 3.0 px with an inefficient detector with  $V = 1/9$  ( $\beta \approx 1736.79 \text{ px}^2$ ). See the text for more details.

the MPD code is very well predicted by the theoretical performance models given in Section 2.

The black dash-dot curves in each panel of Fig. 6 shows the expected median response with a perfect detector; these curves are the same as the solid grey median curves found in Fig. 3. The *observed* stellar intensities and observed background sky level are nine times fainter than was seen in the numerical experiment shown in Fig. 3 and the median photometric and astrometric errors in Fig. 6 are, as expected,  $\sim 3$  ( $= V^{-1/2}$ ) times larger when the inefficient detector is used.

The MPD code and the theoretical performance models work well with PRFs that have volumes of less than 1.

## 5.2 Undersampled discrete PSFs

20 000 *undersampled* CCD stellar observations were simulated using an analytical Gaussian with a FWHM  $\equiv 1.5 \text{ px}$ , the other simulation parameters were the same as given in Section 5.1.1. The median effective background area of PRF of these observations was  $\beta \approx 6.12 \text{ px}^2$  ( $V \equiv 1$ ). All the simulated observations were analysed with MPD using a *discrete* Gaussian PSF with FWHM  $\equiv 1.5 \text{ px}$ .

Fig. 7 shows the absolute photometric errors and total astrometric errors of this numerical experiment. While the photometric and astrometric results for stars with  $\mathcal{E}_{\text{true}} \lesssim 300\,000 \text{ e}^-$  are fine, the results for stars brighter than this limit are seen to quickly degrade in accuracy with the brightest stars having median errors that are  $\sim 40$  times worse than expected.

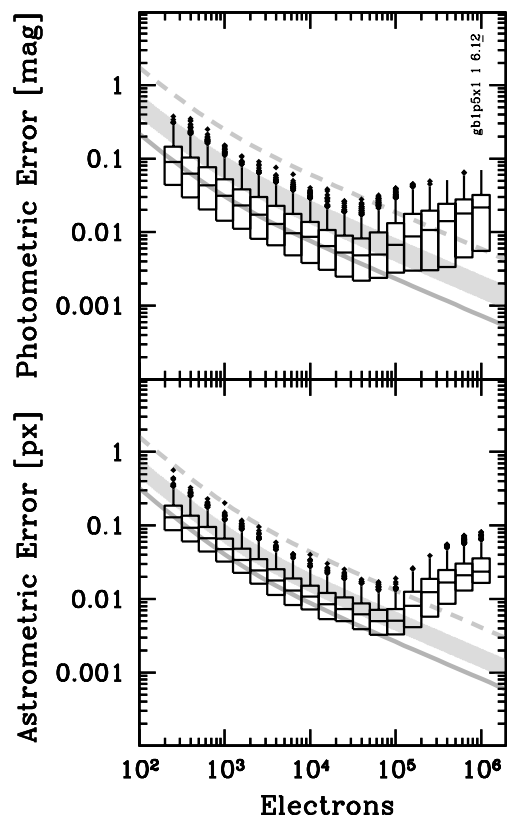


**Figure 7.** The absolute photometric errors (top) and total astrometric errors (bottom) of 20 000 simulated CCD stellar observations analysed with MPD using an undersampled *discrete* Gaussian PSF with a FWHM of 1.5 px ( $\beta \approx 6.12 \text{ px}^2$ ;  $V \equiv 1$ ).

What starts going wrong at  $\mathcal{E}_{\text{true}} \approx 30\,000 \text{ e}^-$ ? Fig. 8 shows a 1-px-wide slice through a pixel-centered discrete Gaussian PSF with FWHM  $= 1.5 \text{ px}$  that was shifted half of a pixel in  $X$  to the right using damped sinc function given in equation (49). The dashed black curve looks fine, but when expanded by a factor of 100, one sees that negative side lobes have been created due to the fact that the Nyquist–Shannon sampling theorem has been violated. Doing a sinc interpolation (damped or otherwise) on undersampled data is never a good idea – the ‘ringing’ seen in Fig. 8 is a classic signature of an edge that is too sharp to be adequately expressed with the limited spatial information contained in an undersampled observation. The biggest negative side lobe of the shifted PSF has a value of about  $-0.0006$ . Although that may seem to be a small value compared to the total volume integral of 1, it is actually quite disastrous because negative PSF values have no physical meaning.

It is now clear what has gone wrong for stars with  $\mathcal{E}_{\text{true}} \gtrsim 30\,000 \text{ e}^-$ . At stellar intensity values greater than 17 000 electrons, the intensity-scaled undersampled PSF models can have negative side lobes that are larger than the rms observed background sky noise level ( $| -0.0006 | \times 17\,000 \text{ e}^- = 10.2 \text{ e}^- > 10 \text{ e}^- \approx \sqrt{B}$ ). At stellar intensity values greater than 167 000 electrons, the observational models have physically nonsensical *negative sky values*.

Aliasing (ringing) effects will generally only be seen with bright stars since a large number of photons are required in order to adequately sample the higher spatial frequencies of a PSF.

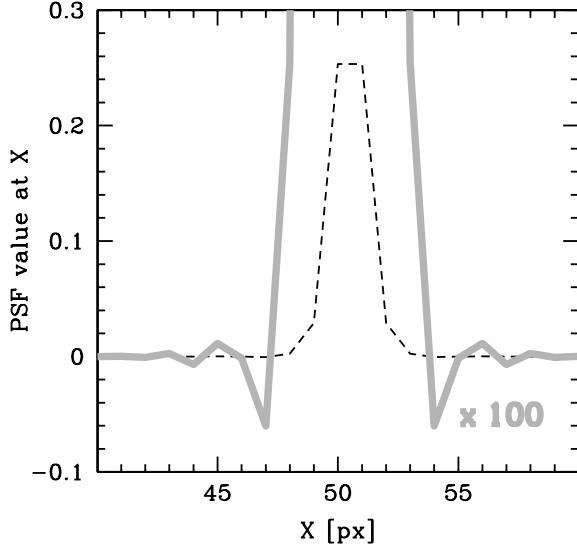


**Figure 8.** A 1-px-wide slice through a pixel-centered discrete Gaussian PSF with FWHM = 1.5 px that was shifted half of a pixel in  $X$  to the right using equation (49). The thick grey curve is the same PSF multiplied by a factor of 100.

Fitting undersampled observations of bright stars with undersampled PSFs results in poor photometry and astrometry.

### 5.3 Supersampled discrete PSFs

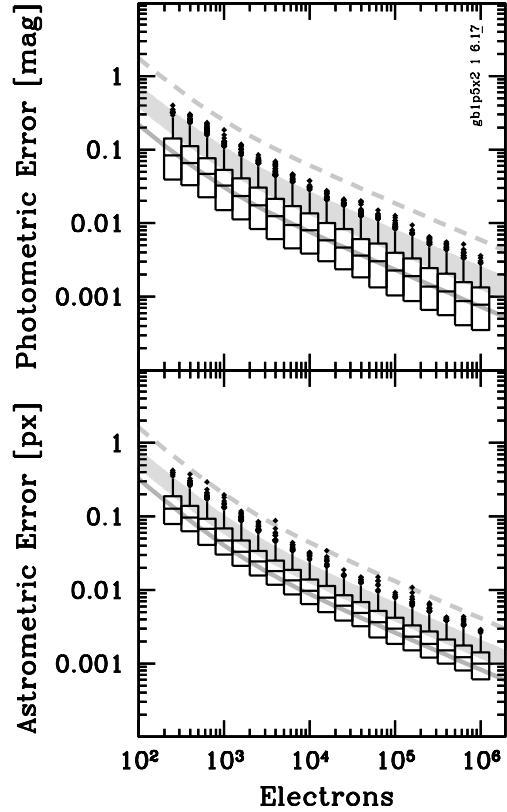
A supersampled PSF is a PSF with pixels that have greater spatial resolution (higher spatial frequencies) than the actual pixels in the observational data. For example, a  $2 \times 2$  supersampled PSF uses four pixels to describe every physical pixel of the CCD observation; each supersampled pixel has twice the spatial resolution of the actual pixels in the observation.

20 000 *undersampled* CCD stellar observations were simulated using an analytical Gaussian with a FWHM  $\equiv 1.5$  px; the other simulation parameters were the same as before. All the simulated observations were analysed with MPD using a  $2 \times 2$  *supersampled* discrete Gaussian PSF with FWHM  $\equiv 1.5$  px ( $\beta \approx 6.17$  px<sup>2</sup>;  $V \equiv 1$ ).

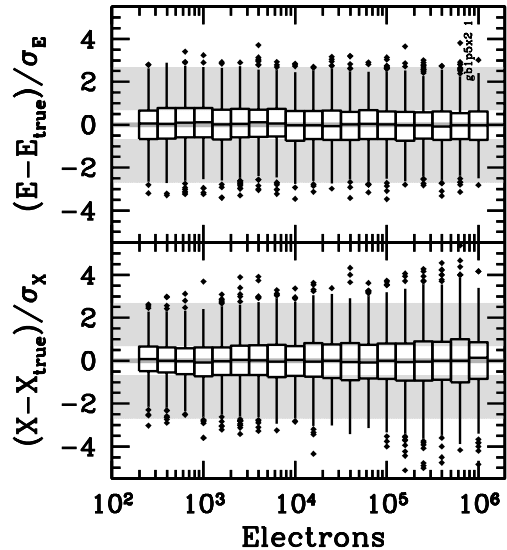
Fig. 9 shows the absolute photometric errors and total astrometric errors of this numerical experiment. By providing MPD with extra information, in the form of a supersampled PSF, the Nyquist–Shannon sampling theorem was no longer violated and excellent photometry and astrometry was done with this undersampled data set.

Fig. 10 shows the relative errors for  $\mathcal{E}$  and  $\mathcal{X}$ . The relative stellar intensity errors are normally distributed. However, the relative  $\mathcal{X}$  position errors are almost, but not quite, normally distributed. The MPD code accurately measures the stellar positions (i.e. the median difference,  $\mathcal{X} - \mathcal{X}_{\text{true}}$ , values are zero), but the rms position error estimates ( $\sigma_{\mathcal{X}}$ ) are slightly *underestimated* (the top and bottom whiskers for  $\mathcal{E}_{\text{true}} \gtrsim 10\,000$  e<sup>−</sup> are seen to extend beyond the grey bands). The same effect is seen with  $\mathcal{Y}$ . Using a higher resolution supersampled PSF ( $3 \times 3$ ,  $4 \times 4$ , ...) does not eliminate the small underestimation by MPD of position errors. The position errors estimated by MPD are close to the photonic limit, but the actual errors – for undersampled observations – are close to the astrometric CRLB with square CCD pixels (Winick 1986).

Accurate and precise CCD stellar photometry and astrometry may be obtained with undersampled CCD observations if supersampled PSFs are used during the PSF-fitting process.



**Figure 9.** The absolute photometric errors (top) and total astrometric errors (bottom) of 20 000 simulated CCD stellar observations analysed with MPD using a  $2 \times 2$  *supersampled* discrete Gaussian PSF with a FWHM of 1.5 px ( $\beta \approx 6.17$  px<sup>2</sup>;  $V \equiv 1$ ).



**Figure 10.** Relative stellar intensity errors (top) and relative  $\mathcal{X}$  position errors (bottom) of the data set used in Fig. 9.

### 5.4 Critically sampled discrete PSFs

Let us now investigate what happens when critically sampled data are fit with a critically sampled PSF.

20 000 *critically sampled* CCD stellar observations were simulated using an analytical Gaussian with a FWHM  $\equiv 2.35482$  px; the other simulation parameters were the same as before. All the

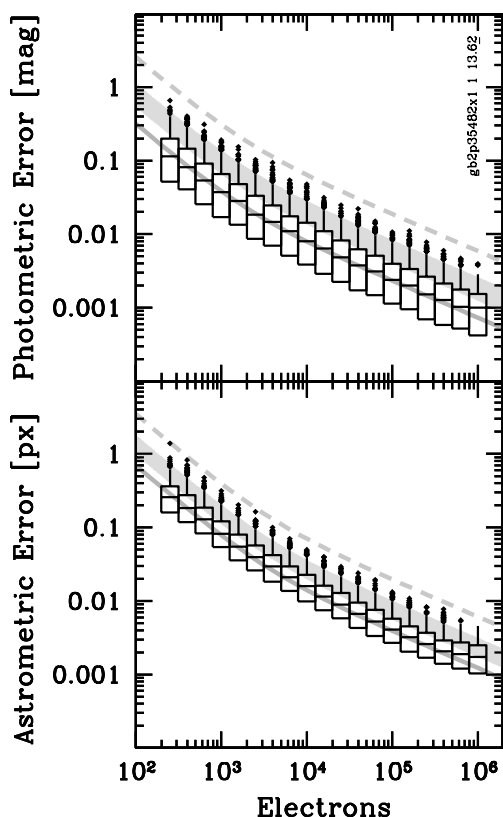


**Figure 11.** The absolute photometric errors (top) and total astrometric errors (bottom) of 20 000 simulated CCD stellar observations analysed with MPD using critically sampled discrete Gaussian PSF with a FWHM of 2.35482 px ( $\beta \approx 13.62 \text{ px}^2$ ;  $V \equiv 1$ ).

simulated observations were analyzed with MPD using a *critically sampled* discrete Gaussian PSF with  $\text{FWHM} \equiv 2.35482 \text{ px}$  ( $\beta \approx 13.62 \text{ px}^2$ ;  $V \equiv 1$ ).

Fig. 11 shows the absolute photometric errors and total astrometric errors of this numerical experiment. Fig. 12 shows the relative errors for  $\mathcal{E}$  and  $\mathcal{X}$ . Looking carefully at Figs 11 and 12, one sees that the photometric and astrometric performance is well matched to the theoretical expectations except for the brightest three bins ( $\mathcal{E}_{\text{true}} \gtrsim 316\,000 \text{ e}^-$ ).

20 000 *critically sampled* CCD stellar observations were simulated using an analytical Gaussian with a  $\text{FWHM} \equiv 2.35482 \text{ px}$ ; the other simulation parameters were the same as before. All the simulated observations were analysed with MPD using a  $2 \times 2$  *supersampled* discrete Gaussian PSF with  $\text{FWHM} \equiv 2.35482 \text{ px}$  ( $\beta \approx 13.62 \text{ px}^2$ ;  $V \equiv 1$ ).

Fig. 13 shows the absolute photometric errors and total astrometric errors of this numerical experiment. Fig. 14 shows the relative errors for  $\mathcal{E}$  and  $\mathcal{X}$ . The photometric and astrometric performance is well matched to the theoretical expectations for all stellar intensities.

Comparing Fig. 7 with Fig. 9 and Fig. 11 with Fig. 13, one sees that one can obtain excellent stellar photometry and astrometry with the MATPHOT algorithm for all stellar intensities – even if the observational data is undersampled – as long as the discrete PSFs used to do the model fitting are sampled finely enough to have sufficient spatial frequency coverage such that the Nyquist–Shannon sampling theorem is not violated.

Comparing Fig. 3 with Fig. 11, one sees that the breakpoint for the MATPHOT algorithm between undersampled and oversampled data is

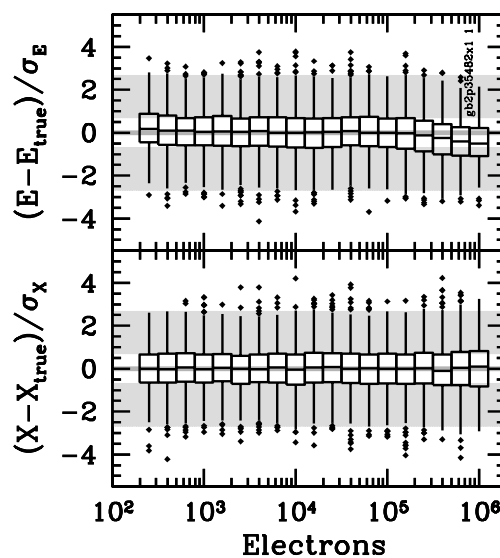


**Figure 12.** Relative stellar intensity errors (top) and relative  $\mathcal{X}$  position errors (bottom) of the data set used in Fig. 11.

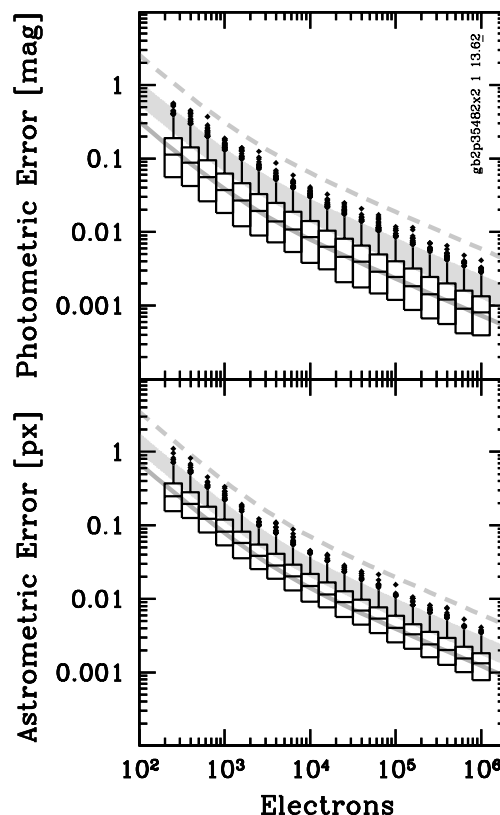


**Figure 13.** The absolute photometric errors (top) and total astrometric errors (bottom) of 20 000 simulated CCD stellar observations analysed with MPD using a  $2 \times 2$  *supersampled* discrete Gaussian PSF with a FWHM of 2.35482 px ( $\beta \approx 13.62 \text{ px}^2$ ;  $V \equiv 1$ ).

$13.62 < \beta \leq 21.44 \text{ px}^2$  or, in terms of a Gaussian FWHM maximum,  $2.35482 \lesssim \text{FWHM} \leq 3 \text{ px}$ .

If a discrete PSF is close to being critically sampled, then one should use a supersampled discrete PSF that is oversampled in terms of supersampled pixels (spx). In other words, if the equivalent-background area is less than 21 square pixels ( $\beta < 21 \text{ px}^2$ ;

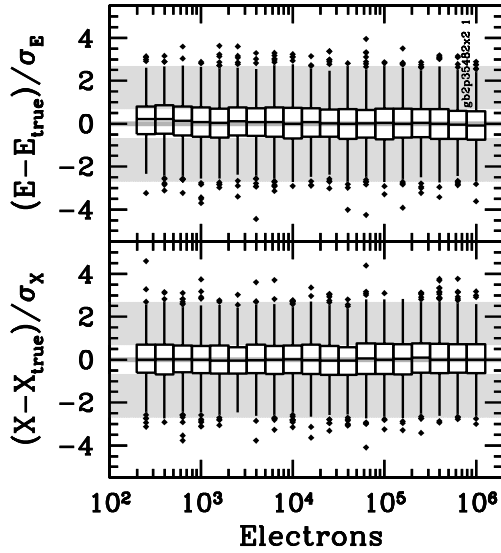


**Figure 14.** Relative stellar intensity errors (top) and relative  $\mathcal{X}$  position errors (bottom) of the data set used in Fig. 13.

Gaussians:  $\text{FWHM} < 3.0 \text{ px}$ ), then one should use a supersampled discrete PSF which has an equivalent-background area of at least 21 square supersampled pixels ( $\beta \geq 21 \text{ spx}^2$ ; Gaussians:  $\text{FWHM} \geq 3.0 \text{ spx}$ ).

### 5.5 Ugly discrete PSFs

Let us now investigate the photometric and astrometric performance of the MATPHOT algorithm with an ugly (realistic) space-based PSF.

Fig. 15 shows a simulated *Next Generation Space Telescope* (NGST) V-band CCD stellar observation. This simulated observa-

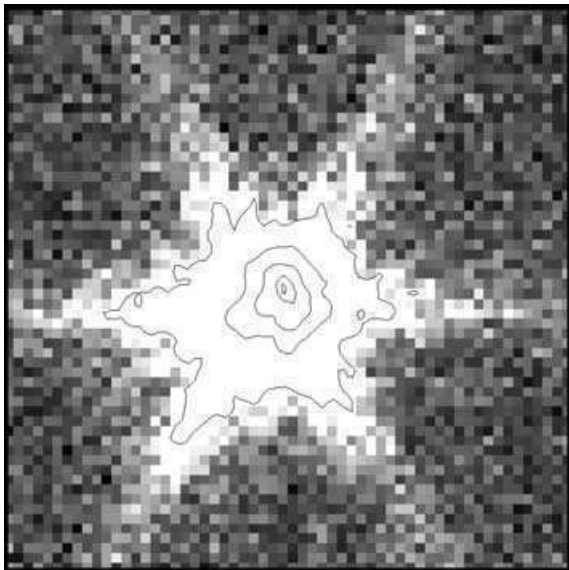


**Figure 15.** A simulated V-band NGST image based on a  $2 \times 2$  supersampled PSF model for a 8-m TRW-concept  $1.5\text{-}\mu\text{m}$  diffraction-limited primary mirror with  $1/13$  rms wave errors. Contour levels of 90, 50, 10, 1 and 0.1 per cent of the peak intensity are shown with black curves. The pixel scale is  $0.0128 \text{ arcsec px}^{-1}$ . This image uses a linear stretch with a pixel intensity mapping of black for  $\lesssim 70 e^-$  and white for  $\gtrsim 150 e^-$ .

tion used a  $2 \times 2$  supersampled PSF, which was based on an 8-m TRW-concept  $1.5\text{-}\mu\text{m}$  diffraction-limited primary mirror with  $1/13$  wave rms errors at  $1.5 \mu\text{m}$ ; the original version of the PSF was kindly provided by John Krist (STScI). The six-sided ‘snowflake’ pattern seen in Fig. 15 is mainly due to the fact that the primary mirror is composed of segmented hexagonal-shaped mirrors. Observers will note that this PSF is very similar to optical PSFs seen with the 10-m telescopes at the W. M. Keck Observatory. The 6.5-m *James Webb Space Telescope* (JWST) is likely to have similar-looking near-infrared PSFs once it achieves first light in  $\sim 2011$ .

The NGST PSF is so complicated that it is unlikely that it could be represented adequately with a continuous analytical mathematical function. Space-based observations frequently have high spatial frequencies, which make them ideal candidates for photometric and astrometric analysis using discrete PSFs.

20 000 CCD stellar observations were simulated using the simulated V-band NGST  $2 \times 2$  supersampled PSF described above; the other simulation parameters were the same as before. All the simulated observations were analysed with MPD and the PSF used to create the simulated observations.

Fig. 16 shows the absolute photometric errors and total astrometric errors of this numerical experiment. Fig. 17 shows the relative errors for  $\mathcal{E}$  and  $\mathcal{X}$ . The photometric and astrometric performance is well matched to the theoretical expectations for all stellar intensities.

Although only Gaussian PSFs were used in previous numerical experiments, the excellent fit seen in the top panel of Fig. 16 between the theoretical photometric performance model (Section 2.3.4) and

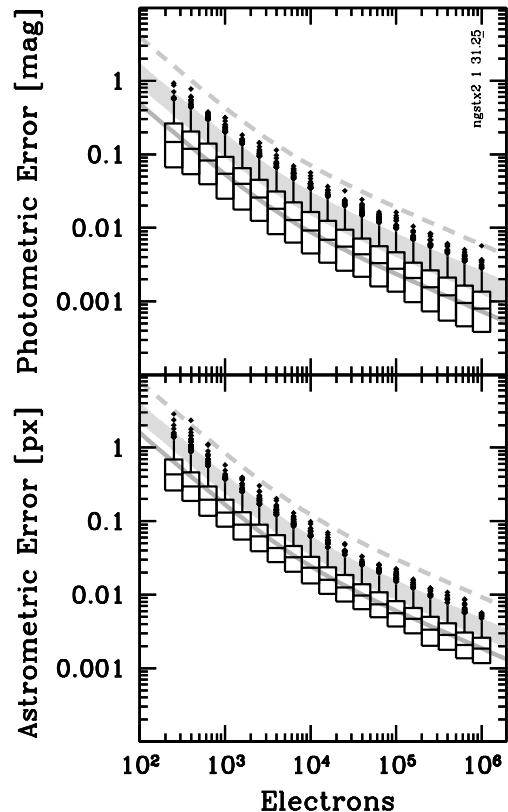


**Figure 16.** The absolute photometric errors (top) and total astrometric errors (bottom) of 20 000 simulated CCD stellar observations analysed with MPD using the  $2 \times 2$  supersampled NGST PSF described in Fig. 15 ( $\beta \approx 31.25 \text{ px}^2$ ;  $V \equiv 1$ ).



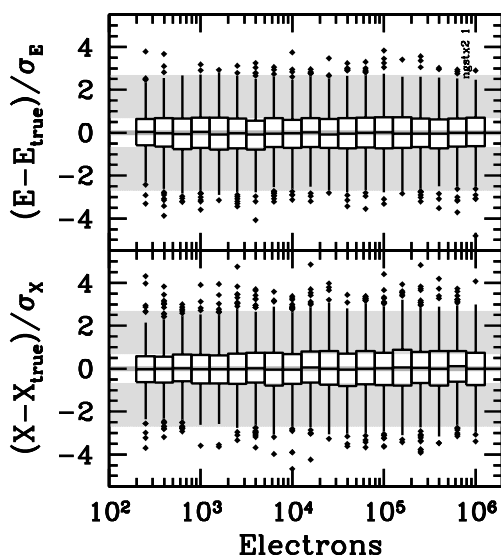


**Figure 17.** Relative stellar intensity errors (top) and relative  $\mathcal{X}$  position errors (bottom) of the data set used in Fig. 16.

actual MPD measurements using such an ugly discrete PSF is not surprising once one remembers that the theoretical photometric performance model was derived from an abstract PRF.

The development of the theoretical astrometric performance model, however, required differentiation of the PRF, which was assumed to be an oversampled analytical Gaussian function. The analytical Gaussian bright star astrometric limit was transformed to the general form by assuming that the Gaussian-specific  $\mathcal{S}^2$  term could be replaced with the more general  $\mathcal{L}^2$  term, which, by definition, can be computed for any PRF. The same assumption was then used to derive the general faint star astrometric limit. The excellent fit seen in the bottom panel of Fig. 16 indicates that this bold assumption is not only useful but practical. Many numerical experiments with very ugly discrete PSFs have shown that the theoretical astrometric performance model of Section 2.4.4 works well with ugly discrete PRFs.

If the MATPHOT algorithm is optimally extracting photometric and astrometric information from a stellar observation, *and* MPD has been correctly coded, *and* the CCD observation has been properly calibrated, *and* the PRF used in the observational model is correct, *and* accurate estimates of the measurements errors for each pixel have been made, *then* one expects that the  $\chi^2$  goodness-of-fit value reported by MPD to be distributed as a  $\chi^2$  distribution with the number of degrees of freedom equal to the difference between the number of pixels in the observation and the number of free parameters. Fig. 18 shows that this prediction about the precision and accuracy of the MATPHOT algorithm has been verified: the cumulative distribution of the  $\chi^2$  reported by MPD (thin black curve) is seen to lie on top of the cumulative  $\chi^2$  distribution of 3596 [= 60<sup>2</sup> pixels – 4 free parameters ( $\mathcal{E}$ ,  $\mathcal{X}$ ,  $\mathcal{Y}$  and  $\mathcal{B}$ )] degrees of freedom (thick grey curve).

The MPD code works well with ugly discrete PSFs and its performance can be well predicted using the general theoretical photometric and astrometric performance models given in Section 2.

The  $\chi^2$  goodness-of-fit value reported by MPD is a statistically reliable measure of the quality of a photometric and astrometric reduction of a stellar observation obtained with the MATPHOT algorithm using ugly discrete PSFs.

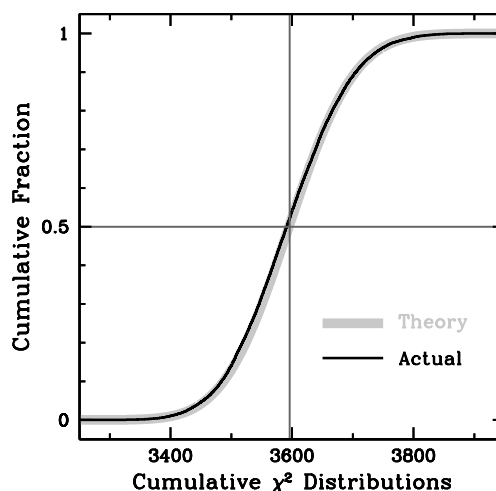


**Figure 18.** A comparison between the cumulative  $\chi^2$  distribution for 3596 degrees of freedom (thick curve) and the measured  $\chi^2$  value (thin curve), of the data set used in Fig. 16, reported by the MPD implementation of the MATPHOT algorithm.

## 5.6 Ugly detectors

Let us now investigate the photometric and astrometric performance of the MATPHOT algorithm with an ugly PSF and an ugly detector.

Suppose one has a detector where every pixel has been divided into 16 square regions called ‘subpixels’. Let us call the first row and first column of subpixels ‘gate structures’, which are optically inactive with 0 per cent QE. The remaining nine subpixels are the optically active part of the pixel with a 100 per cent QE. By definition, such a pixel would have a very large intrapixel QE variation with only 56.25 per cent of the total pixel area being capable of converting photons to electrons.

A few extra lines of code were added to the MPD program to simulate the image formation process with such an ugly detector. The new version of MPD is called MPDX, and was designed specifically for use with  $4 \times 4$  supersampled PSFs.

10000 CCD stellar observations of  $-13$  mag stars ( $\sim 2.512^{13} \gamma$ ) were simulated and analysed with MPDX using a  $4 \times 4$  supersampled version of the simulated V-band NGST PSF described above. The *observed* background level was assumed to be a constant value of  $\mathcal{B} = 56.25 \text{ e}^-$  ( $\mathcal{B}_{\text{true}} = 100 \gamma$ ,  $(V) = 0.5625$ ), and all other simulation parameters were the same as before. The measured PRF volume of these simulated observations was  $V = 0.5616 \pm 0.0185$ , which is consistent with the expected value of 0.5625 from the physical structure of a single pixel. The median and semiquartile range of the effective background area ( $\mathcal{B}$ ) of these observations were, respectively, 28.10 and 4.82 px<sup>2</sup>. The median critical-sampling scale length of these observations was  $\mathcal{L} \approx 0.8398 \text{ px}$  – indicating that these observations were *undersampled*, as expected.

The optically inactive gate structures of the pixel cause the observed number of electrons in each stellar image to be significantly less than the number of photons that fell on the detector. The total amount of loss was dependent on where the centre of the star fell within the central pixel of the stellar image. Fig. 19 shows that stars centred in the middle of the active area of a pixel suffered a  $\sim 40$  per cent loss ( $\Delta m \approx 0.56 \text{ mag}$ ), while those centered on gate structures (grey points) lost up to 47 per cent ( $\Delta m \approx 0.69 \text{ mag}$ ).

Although this numerical experiment may seem to be very artificial, large intrapixel sensitivity variations can be found in cameras

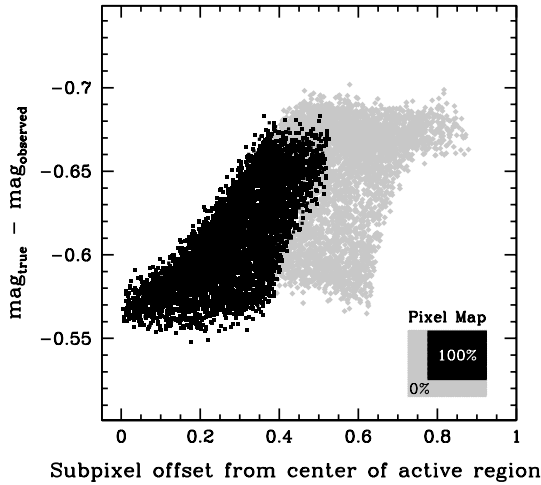


**Figure 19.** The measured electron loss of the 10 000 simulated CCD observations of  $-13$  mag stars analysed with MPDX using a  $4 \times 4$  supersampled version of the *NGST* PSF. The electron loss is plotted as a function of the absolute value of the distance from the centre of a star and the centre of the active region of the central pixel of the stellar image.

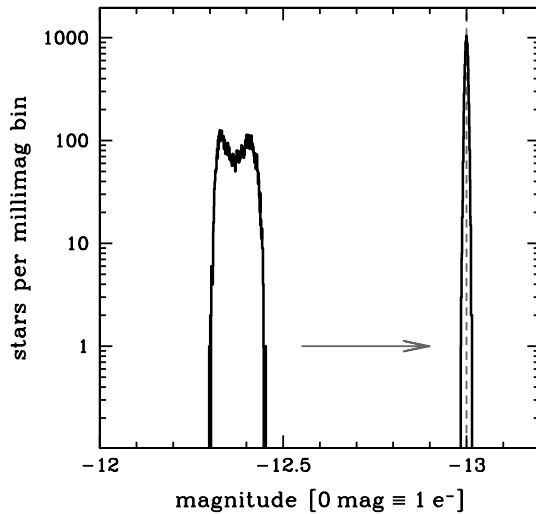


**Figure 20.** The observed (left) and the measured (right) stellar magnitude distributions of the 10 000  $-13$  mag stars described in Fig. 19.

currently installed on the *HST*. Lauer (1999) reported peak-to-peak variations of 0.39 mag at the *J* band (F110W) and 0.22 mag at the *H* band (F160W) of the NIC3 camera of the *HST* NICMOS instrument. The peak-to-peak variation of  $\sim 0.2$  mag at F160W with NIC3 was independently confirmed by Hook & Fruchter (2000).

The mean *observed* stellar magnitude for these  $-13$  mag stars was  $-12.3728 \pm 0.0359$  mag. The photometric performance model predicts an rms measurement error of 0.0036 mag for these bright stars. With an average loss of 44 per cent and an rms measurement error that is *ten times larger* than expected from photon statistics, the observed stellar magnitudes were neither precise nor accurate.

Fig. 20 shows that MPD was able to do an excellent job in recovering the true stellar magnitude of the 10 000  $-13$  mag stars – despite being presented with a worst-case scenario of undersampled observations with an ugly PSF imaged on an ugly detector with a very large intrapixel QE variation.

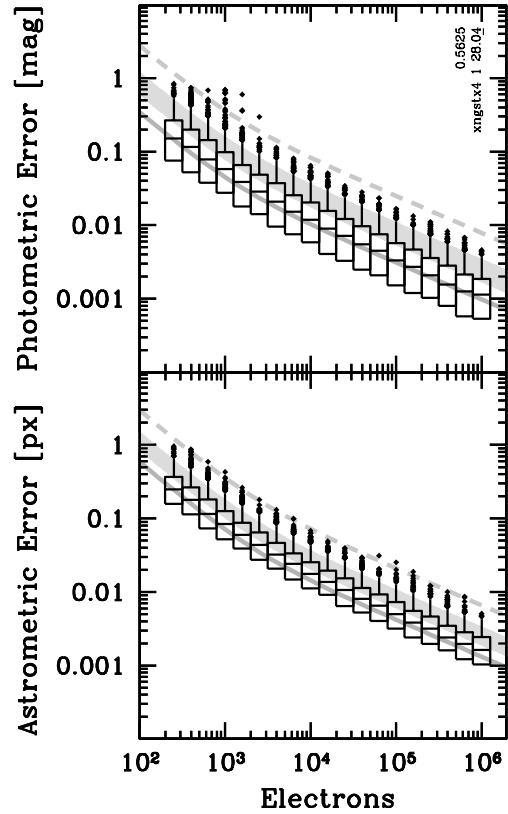


**Figure 21.** The absolute photometric errors (top) and total astrometric errors (bottom) of 20 000 simulated CCD stellar observations analysed with MPDX using a  $4 \times 4$  supersampled version of the *NGST* PSF ( $\beta \approx 28.04$  px<sup>2</sup>;  $V = 0.5625$ ).

The mean *measured* stellar magnitude reported by MPDX was  $-12.9998 \pm 0.0039$  mag and the mean rms error estimated by MPDX was  $0.00384 \pm 0.00006$  mag. The photometric performance of MPDX is fully consistent with theoretical expectations – which were derived for an ideal detector with no intrapixel QE variation.

20 000 CCD stellar observations were simulated and analysed with MPDX using the same  $4 \times 4$  supersampled version of the simulated *V*-band *NGST* PSF. The input stellar intensities ranged from  $-6$  to  $-15$  mag ( $251$  to  $10^6$   $\gamma$ ). The observed background level was assumed to be a constant value of  $B = 56.25$   $e^-$  ( $B_{\text{true}} = 100$   $\gamma$ ,  $\langle V \rangle = 0.5625$ ), and all other simulation parameters were the same as before. The median and semiquartile range of the effective background area ( $\beta$ ) of these observations were, respectively, 28.04 and 4.77 px<sup>2</sup>.

Fig. 21 shows the absolute photometric errors and total astrometric errors of this numerical experiment. Comparing the simulation results with the grey theoretical limits, one sees that the photometric and astrometric performance of the MPDX code is well predicted by the theoretical performance models given in Section 2.

Excellent stellar photometry and astrometry is possible with ugly PSFs imaged onto ugly detectors as long as the image formation process *within the detector* is accurately modelled by the photometric reduction code.

## 6 DISCUSSION

After developing theoretical photometric and astrometric performance model for PSF-fitting stellar photometry, I described the

unique features of the MATPHOT algorithm for accurate and precise stellar photometry and astrometry using discrete PSFs. I conducted numerical experiments with the MPD implementation of the MATPHOT algorithm and demonstrated that the computational noise due to the chosen analysis method (numerical versus analytical) is insignificant when compared to the unavoidable photon noise due to the random arrival photons in any astronomical CCD observation. The MATPHOT algorithm was specifically designed for use with space-based stellar observations where PSFs of space-based cameras frequently have significant amounts of power at higher spatial frequencies. Using simulated *NGST* CCD observations, I demonstrated that mpx relative astrometry and mmag photometry are possible with very complicated space-based discrete PSFs.

The careful reader will observe that I have not discussed *how* a discrete PSF is derived. The MATPHOT algorithm will optimally determine the brightness and position of a star in a CCD observation when provided with the correct PSF and DRF – functions that need to be determined *beforehand* through calibration procedures. Photometric and astrometric accuracy and precision degrades if either the PSF or DRF is poorly known. PSF reconstruction (calibration) is a complicated topic in its own right, and has been the subject of many articles, instrumentation reports and entire workshops. The challenges of PSF reconstruction are many. An astronomer may be faced with trying to derive a PSF from an observation

- (i) with a variable PSF within the field of view,
- (ii) that has too few bright stars,
- (iii) that might be undersampled,
- (iv) that might be poorly dithered,
- (v) that might be poorly flat fielded,
- (vi) that exhibits significant charge transfer efficiency variations,
- (vii) that has variable charge diffusion within the CCD substrate,
- (viii) with significant photon loss due to charge leakage,
- (ix) that might not actually be linear below the 1 per cent level.

While many of these problems can be overcome by the proper design of instruments or experiments, their solution is beyond the scope of this article, which has sought to determine the practical limits of PSF-fitting stellar photometry.

The analysis presented in this article has assumed that PSFs are perfectly known – a situation that is rarely, if ever, physically possible. The *cores* of observationally based PSFs are generally much better determined than the broad *wings* due to simple photon statistics. The effect of large instrumental calibration errors can also be significant. For example, flat-field limitations can dramatically impact the achievable levels of photometric and astrometric precision. An investigation based on theory of PSF errors and flat-field calibration error on the limits of PSF-fitting stellar photometry would be very difficult. An investigation based on numerical experiments, however, might be a much more tractable proposition. In any case, a through investigation of the effects of calibration errors on the limits of PSF-fitting stellar photometry is best left to another article.

## ACKNOWLEDGMENTS

I would like to thank the anonymous referee whose careful reading and insightful comments have improved this article. Special thanks are due to Ian Roederer who checked all of the mathematical proofs in an early draft of the manuscript. Jessica Moy has my heartfelt thanks for cheerfully helping me acquire copies of many articles in technical journals that are not available in the NOAO library collection. I would also like to thank the following people for providing

stimulating conversations, encouragement and support during the extensive research and development effort behind the creation of the MATPHOT algorithm and its various software implementations: Joseph Bredekamp, Susan Hoban, Dot Appleman, Taft Armandroff, Nick Buchholz, Marc Buie, Harvey Butcher, Julian Christou, Chuck Claver, Lindsey Davis, Michele De Le Peña, Mike Fitzpatrick, Ken Freeman, Dan Golombek, Richard Green, Steve Howell, George Jacoby, Buell Jannuzi, Stuart Jefferies, Ivan King, John Krist, Tod Lauer, John MacKenty, John Mather, Mike Merrill, Dave Monet, Mark Morris, Jeremy Mould, Jan Noordam, John Norris, Sudhakar Prasad, the late Alex Rogers, Steve Ridgway, Pat Seitzer, James Schombert, Donald West and Sidney Wolff. This research has been supported in part by the following organizations, institutions and research grants (in reverse chronological order): National Aeronautics and Space Administration (NASA), Interagency order no. S-13811-G, which was awarded by the Applied Information Systems Research Program (NRA 01-OSS-01) of NASA's Science Mission Directorate, Interagency order no. S-67046-F, which was awarded by the Long-Term Space Astrophysics Program (NRA 95-OSS-16) of NASA's Office of Space Science, Center for Adaptive Optics (CfAO), Institute for Pure and Applied Mathematics (IPAM), Kitt Peak National Observatory, National Optical Astronomy Observatory, Association of Universities for Research in Astronomy, Inc. (AURA), National Science Foundation, Mount Stromlo and Siding Spring Observatories, Australian National University, the Netherlands Foundation for Astronomical Research (ASTRON), the Netherlands Organization for the Advancement of Pure Research (ZWO) and the Kapteyn Astronomical Institute of Groningen.

## REFERENCES

- Abramowitz M., Stegun I., 1964, in Abramowitz M., Stegun I., eds, Appl. Math. Ser. Vol. 55, Handbook of Mathematical Functions with Formulas, Graphs, and Mathematical Tables, NBS, Washington, DC
- Arfken G. B. 1970, Mathematical Methods for Physicists, 2nd edn. Academic Press, New York
- Biretta J. et al., 2001, WFPC2 Instrument Handbook, Version 6.0. STScI, Baltimore
- Hook R. N., Fruchter A. S. 2000, in Manset N., Veillet C., Crabtree D., eds, ASP Conf. Ser. Vol. 216, Astronomical Data Analysis Software and Systems IX. Astron. Soc. Pac., San Francisco, p. 521
- Irwin M. J., 1985, MNRAS, 214, 575
- Jakobsen P., Greenfield P., Jedrzejewski R., 1992, A&A, 253, 329
- King I. R., 1971, PASP, 83, 199
- King I. R., 1983, PASP, 95, 163
- Lauer T. R., 1999, PASP, 111, 1434
- Levenberg K., 1944, Q. App. Math., 2, 164
- Marquardt D., 1963, J. SIAM, 11, 431
- Mighell K. J., 1989, MNRAS, 238, 807
- Mighell K. J., 1999, in Mehringer D. M., Plante R. L., Roberts D. A., eds, ASP Conf. Ser. Vol. 172, Astronomical Data Analysis Software and Systems VIII. Astron. Soc. Pac., San Francisco, p. 317
- Mighell K. J., 2002, in Starck J.-L., Murtagh F. D., eds, Proc. SPIE Vol. 4847, Astronomical Data Analysis II. SPIE, Bellingham, WA, p. 207
- Pogson N., 1856, MNRAS, 17, 12
- Perryman M. A. C., Jakobsen P., Colina L., Lelievre G., Macchetto F., Nieto J. L., di Serego Alighieri S., 1989, A&A, 215, 195
- Press W. H., Flannery B. P., Teukolsky S. A., Vetterling W. T., 1986, Numerical Recipes. The Art of Scientific Computing. Cambridge Univ. Press, Cambridge
- Tukey J. W., 1977, Exploratory Data Analysis. Addison-Wesley, Reading, MA
- Wells D. C., Greisen E. W., Harten R. H., 1981, A&AS, 44, 363
- Winick K. A., 1986, JOSA A, 3, 1809

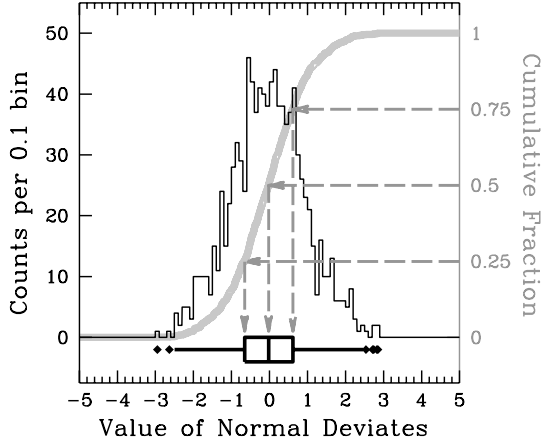


**Figure A1.** A box-and-whiskers plot of a data set of 1000 normal deviates. See the text for details.

## APPENDIX A: BOX-AND-WHISKER PLOTS

A box-and-whisker plot (a.k.a. *box plot*) is a graphical method of showing a data distribution. A box is drawn showing the inner quartile range of the data which, by definition, include half of all the data values (see Fig. A1). The *median* of the data is shown with a bar inside the box. The bottom end of the box is the lower quartile (25 per cent) of the data; Tukey (1977), the creator of the box-and-whiskers plot, calls this value the *lower hinge*,  $LH$ , value. The top end of the box is the upper quartile (75 per cent) of the data, which is called the *upper hinge*,  $UH$ , value. The *step* value is 1.5 times the inner quartile range:  $\Delta \equiv 1.5(UH - LH)$ . The *top fence* value is the sum of the upper hinge and step values:  $TF \equiv UH + \Delta$ . The

*bottom fence* value is the difference between the lower hinge and step values:  $BF \equiv LH - \Delta$ . The *top whisker* is drawn from the upper hinge value to the largest data value that is less than or equal to the top fence value:  $TW \leq TF$ . Similarly, the *bottom whisker* is drawn from the lower hinge value to the smallest data value that is greater than or equal to the bottom fence value:  $BW \geq BF$ . Data values that are greater than the top fence value or less than the bottom fence value are called *outliers* and are plotted at their appropriate value beyond the whiskers. For a normal distribution, which is a Gaussian distribution with a mean of zero and a standard deviation of one, the bottom fence, bottom hinge, median, top hinge and top fence values are, respectively,  $-2.6980$  (0.35 per cent cumulative fraction),  $-0.6745$  (25 per cent),  $0$  (50 per cent),  $0.6745$  (75 per cent),  $2.6980$  (99.65 per cent).

Fig. A1 shows a data set of 1000 normal deviates. The histogram of the data with 0.1-wide bins is shown with thin black lines. The cumulative fraction distribution of the data is shown as a thick grey curve. The box-and-whisker plot of the data is shown with thick black lines below the histogram; arrows show the relationship between various box values and the cumulative fraction distribution. The mean and standard deviation of this data set are,  $-0.0341$  and  $0.9739$ , respectively. The bottom fence, bottom whisker, bottom hinge, median, top hinge, top whisker and top fence values of this data set are, respectively,  $-2.5511$  (0.25 per cent cumulative fraction),  $-2.4940$  (0.30 per cent),  $-0.6522$  (25.10 per cent),  $-0.0231$  (50.00 per cent),  $0.6137$  (75.10 per cent),  $2.4580$  (99.50 per cent),  $2.5126$  (99.57 per cent). The seven outlier values of this data set,  $-2.9500$ ,  $-2.6320$ ,  $2.5390$ ,  $2.7150$ ,  $2.7430$ ,  $2.8270$ ,  $2.8530$ , are plotted in Fig. A1 as diamonds beyond the whiskers.

This paper has been typeset from a  $\text{\TeX}/\text{\LaTeX}$  file prepared by the author.

# FLICKERING RED GIANTS IN THE URSA MINOR DWARF SPHEROIDAL GALAXY: DETECTION OF LOW-AMPLITUDE VARIABILITY IN FAINT RED GIANT BRANCH STARS ON 10 MINUTE TIMESCALES<sup>1</sup>

KENNETH J. MIGHELL<sup>2</sup> AND IAN U. ROEDERER<sup>2,3,4</sup>

National Optical Astronomy Observatory,<sup>5</sup> 950 North Cherry Avenue, Tucson, AZ 85719; mighell@noao.edu, iroedere@indiana.edu

Received 2004 September 13; accepted 2004 October 25; published 2004 November 2

## ABSTRACT

We have analyzed two epochs of *Hubble Space Telescope* Wide Field Planetary Camera 2 observations of the Ursa Minor dwarf spheroidal galaxy using the HSTphot photometric reduction package. We report the detection of nine faint ( $M_V \gtrsim 0.0$  mag) red giant variable stars that exhibit low-amplitude brightness fluctuations on 10 minute timescales with amplitudes ranging from 36 to 130 mmag. We have found variability in 14% of the red giants we have observed. If low-amplitude variability of red giants on 10 minute timescales can be verified and should their numbers prove to be at the 10% level or greater of all red giants in some ancient Population II stellar systems, then the observed color spread of the red giant branch of such systems would be *broadened* by flickering red giants in color-magnitude diagrams based on short (snapshot) observations of a single pair of 10 minute timescale observations in two different filters.

*Subject headings:* galaxies: individual (Ursa Minor dwarf spheroidal) — methods: statistical — stars: variables: other — techniques: photometric

*Online material:* color figures, machine-readable table

## 1. INTRODUCTION

Most stars are variable to some extent. The Sun, for example, is a nonradial pulsator that exhibits brightness fluctuations at the level of  $\sim 3 \times 10^{-6}$  mag (Barban et al. 2004). As stars evolve through the instability strip of the Hertzsprung-Russell diagram, they exhibit periodic pulsations lasting from 1–135 days for classical Cepheids to 5–29 hr for RR Lyraes to 0.2–5 hr for  $\delta$  Scuti stars, with amplitudes ranging from several magnitudes for some bright Cepheid giants to millimagnitudes for some dim  $\delta$  Scuti dwarf stars.

Variability of ancient Population II stars that are cooler (redder) than the right side of the instability strip is an active area of research. While many K and M giant variability studies have concentrated on long-period luminosity changes, with periods from days to years (see, e.g., Eggen 1973; Jorissen et al. 1997; Percy & Polano 1998), most such studies were not designed to detect fast variations with timescales ranging from several minutes to 1 hr. Edmonds & Gilliland’s study of the K giants in the Galactic globular cluster 47 Tucanae with the *Hubble Space Telescope* (HST) Wide Field Planetary Camera 2 (WFPC2) revealed a surprising number of probable variables between the asymptotic giant branch and the red giant branch (RGB) with periods on the order of a few days and  $V$  amplitudes ranging from 5.3 to 14 mmag (Edmonds & Gilliland 1996).

In this Letter, we investigate the level of variability to be found in K giants in nearby dwarf spheroidal (dSph) galaxies with ancient stellar populations. We have analyzed two epochs

of HST observations of the Ursa Minor (UMi) dSph galaxy and report the detection of nine faint ( $M_V \gtrsim 0.0$  mag) red giant variable stars that flicker on 10 minute timescales with  $V$  amplitudes ranging from 36 to 130 mmag.

## 2. OBSERVATIONS AND STELLAR PHOTOMETRY

Two sets of HST WFPC2 observations of the UMi dSph were used in this investigation. The first set of observations (u2pb0101t to u2pb0106t), from the program GTO-6282 (PI: Westphal), was obtained on 1995 July 4 and included three images (each  $\leq 1100$  s) through the F555W ( $\sim V$ ) filter and three images (each  $\leq 1200$  s) through the F814W ( $\sim I$ ) filters. The second set of observations (u5er1301r to u5er1308r), from the program GO-8095 (PI: Ibata), was obtained nearly 4 years later on 1999 July 2 and included four images (each  $\leq 500$  s) in F555W and four images (each  $\leq 500$  s) in F814W. Both sets of observations have similar coverage on the sky since they were obtained with nearly identical target positions and telescope roll angles. These observations were recalibrated using the on-the-fly calibration pipeline at the Canadian Astronomy Data Centre (CADC) and were retrieved by us using guest accounts kindly provided by the CADC.

These observations were reduced using the HSTphot point-spread function (PSF)-fitting stellar photometry package (ver. 1.1; 2003 May) of Dolphin (2000a). Bad pixels were masked using the data quality images. The photometry was performed with the HSTphot program on all images of a particular data set simultaneously. Instrumental magnitudes were transformed to standard  $V$  and  $I$  magnitudes using the calibration solutions described by Dolphin (2000b, 2002a) with updates provided within the HSTphot package. The first F555W image of each data set (1995: u2pb0101t; 1999: u5er1301r) was used as the coordinate reference frame for the identification of all objects in the other images of that data set.

Figure 1 shows the  $V$  versus  $V - I$  color-magnitude diagram for the 1995 observations of the UMi dSph galaxy (similar to Fig. 12 of Dolphin 2002b). Comparing our PSF-fitting photometry of the 1995 data set with the aperture photometry of

<sup>1</sup> Based on observations with the NASA/ESA *Hubble Space Telescope*, obtained from the data archive at the Space Telescope Science Institute, which is operated by the Association of Universities for Research in Astronomy, Inc., under NASA contract NAS 5-26555.

<sup>2</sup> Guest User, Canadian Astronomy Centre, which is operated by the Herzberg Institute of Astrophysics, National Research Council of Canada.

<sup>3</sup> Based on research conducted at NOAO as part of the Research Experiences for Undergraduates Program.

<sup>4</sup> Current address: Department of Astronomy, Indiana University, Swain Hall West 319, 727 East Third Street, Bloomington, IN 47405-7105.

<sup>5</sup> Operated by the Association of Universities for Research in Astronomy, Inc., under cooperative agreement with the National Science Foundation.

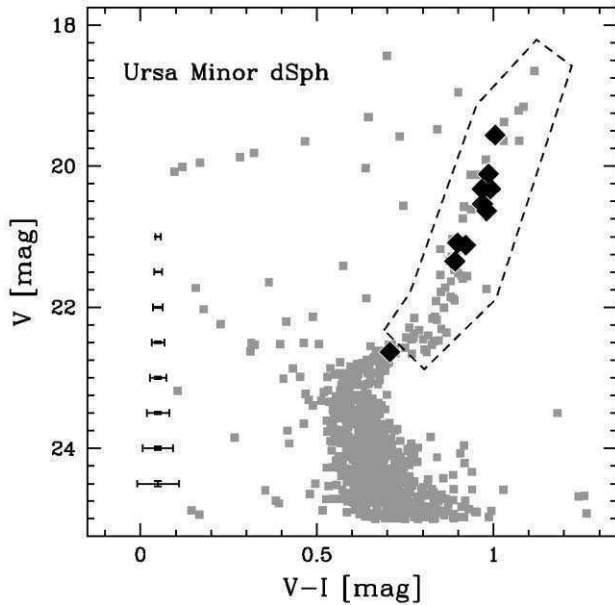


FIG. 1.— $V$  vs.  $V - I$  color-magnitude diagram for the 1995 observations of the UMi dSph galaxy. The error bars indicate typical rms ( $1\sigma$ ) uncertainties for a single star at the corresponding magnitude. There are 852 stars down to the limiting magnitude of  $V = 25.0$ ; a total of 65 red giants are found within the dashed region enclosing the observed portion of the RGB (the top of the RGB was lost as a result of saturation). The 10 low-amplitude variable candidates, described in § 3, are shown as big diamonds. [See the electronic edition of the *Journal* for a color version of this figure.]

Mighell & Burke (1999), we find that our  $V$  magnitudes are slightly fainter ( $\Delta V_{\text{MR-MB}} = 0.040 \pm 0.015$  mag) and our  $V - I$  colors are slightly redder [ $\Delta(V - I)_{\text{MR-MB}} = 0.030 \pm 0.020$  mag] than that of Mighell & Burke.

### 3. FLICKERING LOW-AMPLITUDE RED GIANT VARIABLES

Candidate variables were selected from the HSTphot output using the following  $\chi^2$ -based test statistic,  $\chi_{V+I}^2 \equiv \chi_V^2 + \chi_I^2$ , which combines a variability test statistic in the  $V$  filter,  $\chi_V^2 \equiv \sum_{j=1}^{N_V} (V_j - \langle V \rangle)^2 / (\sigma_{V_j}^2 + 0.01^2)$ , with a variability test statistic in the  $I$  filter,  $\chi_I^2 \equiv \sum_{j=1}^{N_I} (I_j - \langle I \rangle)^2 / (\sigma_{I_j}^2 + 0.01^2)$ , where  $N_V$  ( $N_I$ ) is the number of images obtained with the F555W (F814W) filter,  $V_j$  ( $I_j$ ) is the standard magnitude of the  $j$ th observation,  $\sigma_{V_j}$  ( $\sigma_{I_j}$ ) is the matching rms measurement error, and  $\langle V \rangle$  ( $\langle I \rangle$ ) is the average magnitude of all observations with a given filter. A small error of 0.01 mag has been added in quadrature to account

for a minimum image-to-image photometric scatter of 0.01 mag (see, e.g., Holtzman et al. 1995a, 1995b; Stetson 1998; Dolphin 2000a; Pritzl et al. 2003). We required that each candidate variable be classified by HSTphot as a “good star” (class = 1) and have an rms measurement error of 0.10 mag or less in *all observations of a given epoch* of observation. These selection criteria yielded a subset 157 stars from the 1995 photometry and a subset 216 stars in the 1999 photometry.

Two *independent* sets of variable candidates from the subsets of the 1995 and 1999 photometry were then made by selecting all stars with  $\chi_{V+I}^2$  values greater than 9.49 and 12.59, respectively (Abramowitz & Stegun 1964, p. 985;  $Q = 0.05$  and  $\nu = 4$  and 6). We found a total of 31 and 29 potential variable candidates, respectively, at the 95% confidence level in the 1995 and 1999 observations with an average  $V$  magnitude brighter than 22.8 mag, which is approximately the mean brightness of the subgiant branch of the UMi dSph galaxy. We found a total of 11 candidates that appeared on *both* lists; nine are stars on UMi’s RGB (see Fig. 1), one is a subgiant branch star, and the remaining object has a  $V - I$  color of  $2.475 \pm 0.027$  mag and a  $V$  magnitude of  $20.951 \pm 0.016$ , which suggests that it is a distant galaxy or a quasar.

The photometry of the nine red giant variable candidates for both observation epochs is given in Table 1. Lines 1–36 give the 1995 photometry and lines 37–72 give the 1999 photometry, with four lines per star per epoch. The amplitudes  $A_V$  and  $A_I$ , given in Table 1, are defined as being the difference between the faintest and brightest magnitude measurements for  $V$  and  $I$ , respectively, in a given observation epoch. Light curves in  $V$  and  $I$  of four of the nine RGB variable candidates are given in Figure 2.

How believable are the reported photometric errors of HSTphot? If the photometric errors reported by HSTphot are accurate, then the cumulative distribution of the difference between many observations of a star and its average magnitude divided by the reported photometric error should be equivalent to the cumulative distribution of a Gaussian with a mean of zero and a standard deviation of 1 (also known as the cumulative normal distribution; see the dashed curve of Fig. 3). We selected a subset of 952 measurements of stars from the 1999 HSTphot photometry that were *not* variable at the 90% confidence level ( $\chi_V^2$  or  $\chi_I^2 \leq 6.251$ ;  $Q = 0.1$  and  $\nu = 3$ ). The jagged thin dark curve in Figure 3 shows the cumulative distribution of the difference between the HSTphot magnitude of the nonvariable and the average HSTphot magnitude divided by the *softened photometric error*, which is defined to be the reported HSTphot magnitude error added in quadrature to a small image-to-image error of 0.01 mag. These

TABLE 1  
PHOTOMETRY OF THE RGB VARIABLE CANDIDATES

Name	ID <sup>a</sup>	1	$A_V$	$\langle V \rangle$	$V_1$	$V_2$	$V_3$	$V_4$
		2	$\chi_V$	$\sigma_{\langle V \rangle}$	$\sigma_{V_1}$	$\sigma_{V_2}$	$\sigma_{V_3}$	$\sigma_{V_4}$
		3	$A_I$	$\langle I \rangle$	$I_1$	$I_2$	$I_3$	$I_4$
		4	$\chi_I$	$\sigma_{\langle I \rangle}$	$\sigma_{I_1}$	$\sigma_{I_2}$	$\sigma_{I_3}$	$\sigma_{I_4}$
RGB1 .....	173764892	1	0.036	20.323	20.338	20.339	20.303	...
		2	5.58	0.004	0.014	0.006	0.006	...
		3	0.111	19.331	19.417	19.306	19.345	...
		4	29.32	0.004	0.015	0.005	0.005	...

NOTES.—Table 1 is published in its entirety in the electronic edition of the *Astrophysical Journal Letters*. A portion is shown here for guidance regarding its form and content.

<sup>a</sup> The leftmost digit of the identification gives the WFPC2 CCD number (1, 2, 3, or 4, for cameras PC1, WF2, WF3, or WF4, respectively) where the star was found in the first F555W observation of each epoch of observation (1995: u2pb0101t; 1999: u5er1301r). The rightmost four digits give the  $x$ -coordinate of the star multiplied by 10. The remaining four digits give the  $y$ -coordinate of the star multiplied by 10. For example, the first star has an ID of 173764892, indicating that it is found on the PC1 image at the  $(x, y)$  location of (489.2, 737.6).

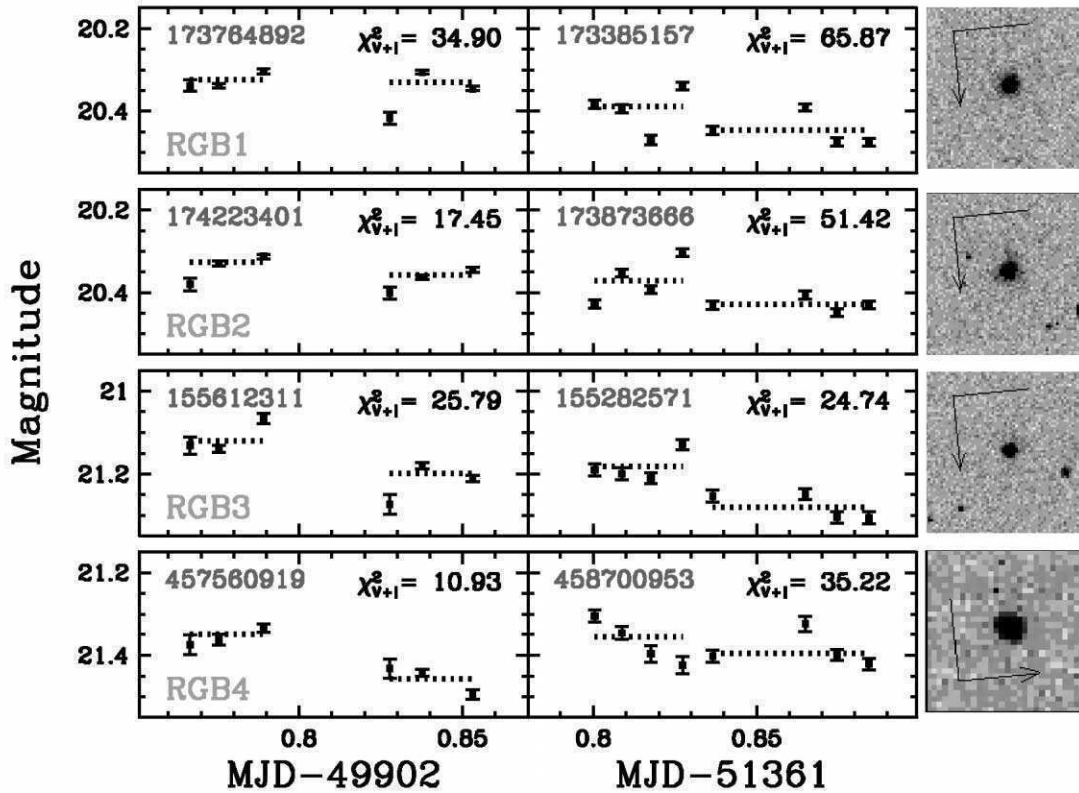


FIG. 2.—Light curves for four of the nine low-amplitude RGB variable candidates in the UMi dSph galaxy. Each row gives the 1995 (*left*) and 1999 (*right*) light curves and a finding chart for a given RGB variable candidate (see Table 1). The first set of points, for a given observation epoch, is the V light curve; the second shows the I light curve plotted 1 mag fainter. The variable name is shown in the bottom left-hand corner of each row. The positional identifier and the value of the  $\chi^2_{V+I}$  statistic is shown, respectively, in the top left-hand and top right-hand corner of each box, for each observation epoch. The finding charts have a small field of view of  $3'' \times 3''$ , with the arrow of the compass pointing north and the line pointing east. Note that these are not crowded star fields. The time value is the Modified Julian Date (MJD) of the middle of the observation; add 2,400,000.5 to get the Julian Date. [See the electronic edition of the Journal for a color version of this figure.]

distributions are highly likely to be different; the Kolmogorov-Smirnov (K-S) statistic probability that the underlying distributions described by the jagged and dashed curves are the *same* is just 0.2%. Note that the jagged curve of Figure 3 lies *below* that of the dashed curve for *negative* values and *above* that of the dashed curve for *positive* values. This implies that *softened* HSTphot

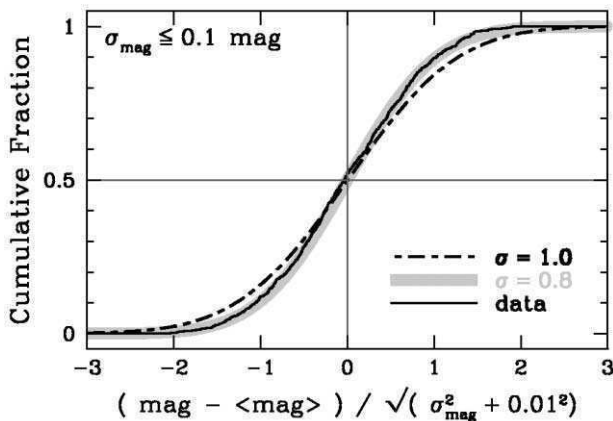


FIG. 3.—Statistical test of HSTphot photometric errors. Softened HSTphot photometric errors are conservative in that they typically overestimate the true error by  $\sim 25\%$ . See the text for details. [See the electronic edition of the Journal for a color version of this figure.]

*photometric errors are conservative*. How conservative? Note that the jagged curve is well modeled by the thick curve, which is a cumulative distribution of a Gaussian with a mean of zero and a standard deviation of 0.8 ( $\sigma = 0.8$ ). These distributions are *statistically consistent*; the K-S statistic probability that the underlying distributions described by the jagged and thick curves are the *same* is 30.2%—which is much greater than the standard rejection level of  $\leq 5\%$ . Remembering that the K-S test is a negative test, we conclude that *softened* HSTphot photometric errors are *overestimated* by  $\sim 25\%$ . Considering that the definitions of our variability statistics for V and I used softened HSTphot errors, the actual probabilities for variability of the nine RGB variable candidates given in Table 1 are probably higher than suggested by their tabulated  $\chi^2_V$  and  $\chi^2_I$  values.

Our claim that the softened HSTphot photometric errors are overestimated by about 25% has been verified using a substantially larger data set of another astronomical target. We analyzed all of the F555W and F814W exposures of the program GO-6114 (PI: Renzini), which were originally used to study the white dwarf cooling sequence of 47 Tuc (see Zoccali et al. 2001). We found 1070 nonvariable stars that had rms measurement errors of 0.10 mag or less in all 10 F555W and all 10 F814W observations in this data set ( $\chi^2_V$  or  $\chi^2_I \leq 14.6837$ :  $Q = 0.1$  and  $\nu = 9$ ). We computed, as above, the difference between a measurement of the stellar magnitude and its average HSTphot magnitude divided by the softened photometric error. If the softened

photometric errors are overestimated by 25%, then we expect the mean and standard deviation of this distribution to be, respectively, zero ( $\bar{x} \equiv 0$ ) and  $\sigma \equiv 0.8$ ; we measured statistically consistent values of  $\bar{x} = -0.0298$  and  $\sigma = 0.8133$ . Bright stars ( $S/N > 10$ ) have softened HSTphot photometric errors that are overestimated by a factor of about 25%.

#### 4. SUMMARY AND DISCUSSION

Our conservative statistical analysis of HSTphot photometry of two epochs of *HST* WFPC2 observations of the UMi dSph galaxy has yielded the detection of nine faint ( $M_V \gtrsim 0.0$  mag) red giant variable stars that exhibit low-amplitude brightness fluctuations on 10 minute timescales with amplitudes ranging from 36 to 130 mmag. We have found variability in 14% of the red giants we have observed (nine out of 65; see Fig. 1).

Are these detections purely statistical flukes? While a statistical possibility, such an explanation is highly improbable. Variability in each of these nine stars was detected *independently in two epochs of observations* separated by nearly 4 years in time. Different parts of the WFPC2 cameras were used to make these observations: the 1999 observations were dithered, but the 1995 observations were not. And while we may have found a previously undetected problem within the WFPC2 cameras or calibrations, the large body of published Local Group stellar population studies conducted with the WFPC2 instrument suggests that instrumental problems at this level would likely have been previously found.

If there is nothing wrong with the actual observations, then could there be something wrong with HSTphot? Figure 3 indicates that image-to-image accuracy of the photometry of nonvariable stars is excellent and conservative. Significant systematic image-to-image measurement errors by HSTphot—including problems with charge transfer efficiency and aperture corrections—would have been detected during the statistical tests of nonvariable stars described above. False detections by HSTphot, while possible, seem to be rather unlikely.

Are these flickering red giants exhibiting periodic variability? The small number and timing of these observations precludes any quantitative analysis for periodicity in these flickering red giants. Note that the amplitudes reported here may only be lower limits of the true amplitudes. Given this poor state of our current understanding of the actual nature of the brightness fluctuations in these red giant variables, any discussion of the source of variability is purely speculative.

The underlying phenomenon responsible for flickering faint red giants is likely to be different than that for the K giant variables (KGVs) found by Edmonds & Gilliland (1996) near the region of the RGB *heap* of 47 Tuc (Bedin et al. 2000). The KGVs probably vary on timescales that are much longer than 10 minutes.

Edmonds & Gilliland (1996) did not find any faint low-

amplitude red giants in 47 Tuc with variability on 10 minute timescales. Although they had excellent 6–7 mmag photometry for stars on the horizontal branch, the photometric errors for faint RGB stars were considerably higher (~10–40 mmag; see Figs. 10 and 4 of Edmonds et al. 1996). The unambiguous detection of low-amplitude variability in red giant variables generally requires excellent photometry with errors of 20 mmag or better. Given that the flickering UMi red giants have a median semiamplitude value of 29 mmag, the detection of flickering faint red giants in 47 Tuc would likely have been difficult with the *U*-band (F336W) *HST* Planetary Camera data set used by Edmonds & Gilliland.

If the timescale of the source of variability is a few years or less, then the flickering of red giants could possibly be seen to turn on and off during a multiyear high-precision space-based photometric survey by NASA's *Kepler* planet-finder mission or the next generation of ground-based digital sky survey projects like Pan-STARRS or the Large Synoptic Survey Telescope. Instead of waiting for those projects to achieve first light, ground-based high-precision follow-up studies could be conducted today with short 3–5 minute exposures using the latest generation of CCD cameras, like the OPTIC camera (Howell et al. 2003), which is based on orthogonal transfer CCDs, at a 4 m class telescope, like the 3.5 m WIYN telescope at the Kitt Peak National Observatory.

If flickering of red giants on 10 minute timescales can be verified and should their numbers prove to be at the 10% level or greater of all red giants in some ancient Population II stellar systems, then the observed color spread of the RGB of such systems would be *broadened* by flickering red giants in color-magnitude diagrams based on short (snapshot) observations of a single pair of 10 minute timescale observations in two different filters (e.g., GO-8192, GO-8601). One expects that any possible overestimation of the length of star formation bursts due to flickering faint red giants would be minimal because state of the art star formation history studies are based on the average colors derived from total exposure times that are generally much longer than 10 minutes.

K. J. M. was supported by a grant from the National Aeronautics and Space Administration (NASA), Interagency Order No. S-13811-G, which was awarded by the Applied Information Systems Research Program (NRA 01-OSS-01) of NASA's Science Mission Directorate (formerly known as the Office of Space Science). I. U. R. was supported by the NOAO/KPNO Research Experiences for Undergraduates (REU) Program, which is funded by the National Science Foundation through Scientific Program Order No. 3 (AST-0243875) of the Cooperative Agreement No. AST-0132798 between the Association of Universities for Research in Astronomy and the NSF. This research has made use of NASA's Astrophysics Data System Abstract Service.

#### REFERENCES

- Abramowitz, M., & Stegun, I., eds. 1964, *Handbook of Mathematical Functions with Formulas, Graphs, and Mathematical Tables* (Washington, DC: NBS)
- Barban, C., Hill, F., & Kras, S. 2004, *ApJ*, 602, 516
- Bedin, L. R., et al. 2000, *A&A*, 363, 159
- Dolphin, A. E. 2000a, *PASP*, 112, 1383
- . 2000b, *PASP*, 112, 1397
- . 2002a, in *The 2002 HST after the Installation of the ACS and the NICMOS Cooling System*, ed. S. Arribas, A. Koekemoer, & B. Whitmore (Baltimore: STScI), 303
- . 2002b, *MNRAS*, 332, 91
- Edmonds, P. D., & Gilliland, R. L. 1996, *ApJ*, 464, L157
- Edmonds, P. D., et al. 1996, *ApJ*, 468, 241
- Eggen, O. J. 1973, *ApJ*, 184, 793
- Holtzman, J. A., et al. 1995a, *PASP*, 107, 156
- . 1995b, *PASP*, 107, 1065
- Howell, S. B., Everett, M. E., Tonry, J. L., Pickles, A., & Dain, C. 2003, *PASP*, 115, 1340
- Jorissen, A., Mowlavi, N., Sterken, C., & Manfroid, J. 1997, *A&A*, 324, 578
- Mighell, K. J., & Burke, C. J. 1999, *AJ*, 118, 366
- Percy, J. R., & Polano, S. 1998, in *ASP Conf. Ser. 135, A Half-Century of Stellar Pulsation Interpretations*, ed. P. A. Bradley & J. A. Guzik (San Francisco: ASP), 249
- Pritzl, B. J., et al. 2003, *AJ*, 126, 1381
- Stetson, P. B. 1998, *PASP*, 110, 1448
- Zoccali, M., et al. 2001, *ApJ*, 553, 733



## **QLWFPC2: Parallel-Processing Quick-Look WFPC2 Stellar Photometry Based on the Message Passing Interface**

Kenneth John Mighell

*National Optical Astronomy Observatory, 950 North Cherry Avenue,  
Tucson, AZ 85719*

**Abstract.** I describe a new parallel-processing stellar photometry code called QLWFPC2 (<http://www.noao.edu/staff/mighell/qlwfpc2>) which is designed to do quick-look analysis of two entire WFPC2 observations from the Hubble Space Telescope in under 5 seconds using a fast Beowulf cluster with a Gigabit-Ethernet local network. This program is written in ANSI C and uses MPICH implementation of the Message Passing Interface from the Argonne National Laboratory for the parallel-processing communications, the CFITSIO library (from HEASARC at NASA's GSFC) for reading the standard FITS files from the HST Data Archive, and the Parameter Interface Library (from the INTEGRAL Science Data Center) for the IRAF parameter-file user interface. QLWFPC2 running on 4 processors takes about 2.4 seconds to analyze the WFPC2 archive datasets u37ga407r.c0.fits (F555W; 300 s) and u37ga401r.c0.fits (F814W; 300 s) of M54 (NGC 6715) which is the bright massive globular cluster near the center of the nearby Sagittarius dwarf spheroidal galaxy. The analysis of these HST observations of M54 lead to the serendipitous discovery of more than 50 new bright variable stars in the central region of M54. Most of the candidate variables stars are found on the PC1 images of the cluster center — a region where no variables have been reported by previous ground-based studies of variables in M54. This discovery is an example of how QLWFPC2 can be used to quickly explore the time domain of observations in the HST Data Archive.

### **1. Motivation**

Software tools which provide *quick-look data analysis* with *moderate accuracy* (3–6 percent relative precision) could prove to be very powerful data mining tools for researchers using the U.S. National Virtual Observatory (NVO).

The NVO data server may also find quick-look analysis tools to be very useful from a practical operational perspective. While quick-look stellar photometry codes are excellent tools to create metadata about the contents of CCD image data in the NVO archive, they also can provide the user with *real-time analysis of NVO archival data*.

It is significantly *faster to transmit* to the NVO user *a quick-look color-magnitude diagram* (consisting of a few kilobytes of graphical data) *than it is*

to transmit the entire observational data set which may consist of 10, 100, or more megabytes of data. By judiciously expending a few CPU seconds at the NVO data server, an astronomer using the NVO might well be able to determine whether a given set of observations is likely to meet their scientific needs.

Quick-look analysis tools thus could provide a better user experience for NVO researchers while simultaneously allowing the NVO data servers to perform their role more efficiently with better allocation of scarce computational resources and communication bandwidth.

Successful quick-look analysis tools must be fast. Such tools must provide useful information in just a few seconds in order to be capable of improving the user experience with the NVO archive.

## 2. QDPHOT

The MXTOOLS<sup>1</sup> package for IRAF has a fast stellar photometry task called QDPHOT (Quick & Dirty PHOTometry) which quickly produces good (about 5% relative precision) CCD stellar photometry from 2 CCD images of a star field. For example, QDPHOT takes a few seconds to analyze 2 Hubble Space Telescope WFPC2 frames containing thousands of stars in Local Group star clusters (Mighell 2000). Instrumental magnitudes produced by QDPHOT are converted to standard colors using the MXTOOLS task WFPC2COLOR.

## 3. QLWFPC2

I have recently implemented a parallel-processing version of the combination of the QDPHOT and WFPC2COLOR tasks using the MPICH<sup>2</sup> implementation of the Message Passing Interface (MPI) from the Argonne National Laboratory.

This new stand-alone multi-processing WFPC2 stellar photometry task is called QLWFPC2<sup>3</sup> (Quick Look WFPC2) and is designed to analyze two complete WFPC2 observations of Local Group star clusters in less than 5 seconds on a 5-node Beowulf cluster of Linux-based PCs with a Gigabit-Ethernet local network. QLWFPC2 is written in ANSI C and uses the CFITSIO<sup>4</sup> library (from HEASARC at NASA's Goddard Space Flight Center) to read FITS images from the HST Data Archive, and the Parameter Interface Library (PIL<sup>5</sup>) (from the INTEGRAL Science Data Center) for the IRAF parameter-file user interface.

---

<sup>1</sup><http://www.noao.edu/staff/mighell/mxtools>

<sup>2</sup><http://www-unix.mcs.anl.gov/mpi/mpich>

<sup>3</sup><http://www.noao.edu/staff/mighell/qlwfpc2>

<sup>4</sup><http://heasarc.gsfc.nasa.gov/docs/software/fitsio>

<sup>5</sup>[http://isdc.unige.ch/bin/std.cgi?Soft/isdc\\_releases\\_public\#osa-2.0](http://isdc.unige.ch/bin/std.cgi?Soft/isdc_releases_public\#osa-2.0)

#### 4. QLWFPC2 Performance

The current implementation of QLWFPC2 was tested on a Beowulf cluster composed of 5 single 1.8-GHz AMD Athalon CPUs with 3 GB total memory interconnected with a Gigabit-Ethernet local network and 120 GB of NFS-mounted disk and an additional 40 GB of local disk.

QLWFPC2 running on 4 processors takes about 2.4 seconds (see Figure 1) to analyze the WFPC2 archive data sets u37ga407r.c0.fits (filter: F555W; exposure: 300 s) and u37ga401r.c0.fits (filter: F814W; exposure: 300 s) of M54 which is the bright massive globular cluster near the center of the Sagittarius dwarf spheroidal galaxy. QLWFPC2 analyzed over 50,000 point source candidates and reported V, I, F555W and F814W photometry of 14,611 stars with signal-to-noise ratios of 8 or better.

The analysis of these HST observations of M54 lead to the serendipitous discovery of more than 50 new bright variable stars in the central region of M54 (Mighell & Schlafman 2004). Most of the candidate variables stars are found on the PC1 images of the cluster center — a region where no variables have been reported by previous ground-based studies of variables in M54. This discovery is an example of how QLWFPC2 can be used to quickly explore the time domain of observations in the HST Data Archive.

#### 5. Recommendations

- **Buy fast machines.** QLWFPC2 almost met the design goal of 5 seconds with a single CPU. Note that a very large number of machines operating at less than 1 GHz would not be able to meet the 5 second design goal.
- **Buy fast networks.** *Gigabit Ethernet is ideally suited for today's GHz-class CPUs and is now very affordable.* Old networks operating at Fast Ethernet speeds will be bandwidth-bound for tasks requiring large (> 1 MB) messages. The test Beowulf cluster has a latency of 90 microseconds and a sustained bandwidth of 33 MB/s for large messages.
- **Buy fast disks.** The main disk of the test Beowulf cluster can read large FITS files at a respectable 30 MB/s with 7200 rpm disks. Nevertheless, reading two WFPC2 images still takes 0.6 seconds to read — which is a significant fraction of the measured total execution times.

**Acknowledgments.** This work is supported by a grant from the National Aeronautics and Space Administration (NASA), Interagency Order No. S-13811-G, which was awarded by the Applied Information Systems Research Program (AISRP) of NASA's Office of Space Science (NRA 01-OSS-01).

#### References

- Mighell, K. J. 2000, in ASP Conf. Ser., Vol. 216, ADASS IX, ed. N. Manset, C. Veillet, & D. Crabtree (San Francisco: ASP), 651
- Mighell, K. J. , & Schlafman, K. C. 2004 (in preparation).

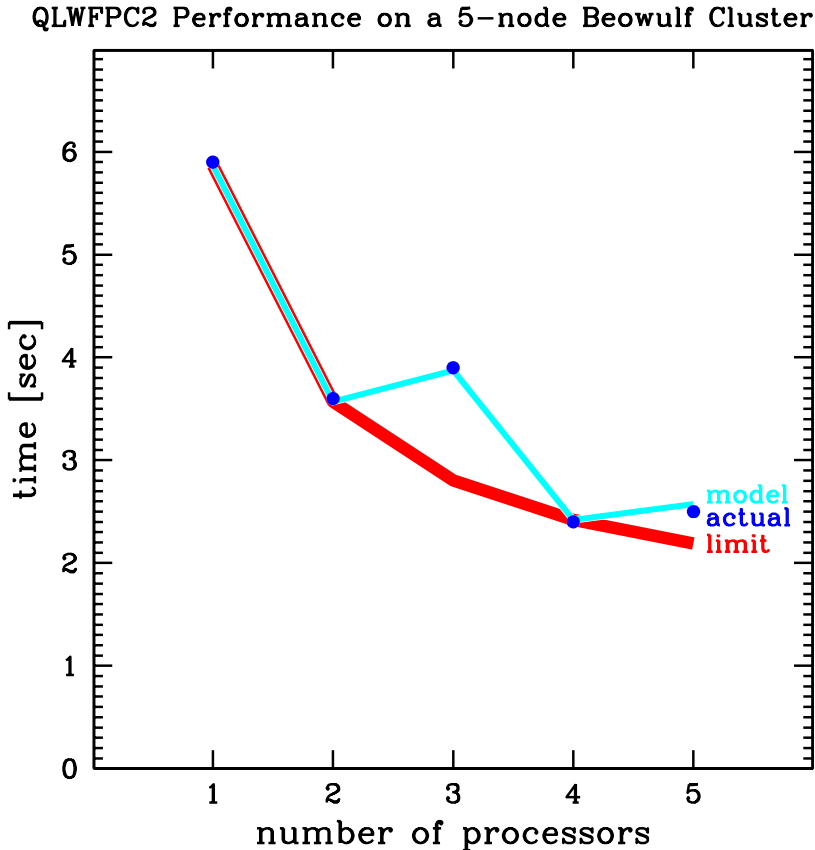


Figure 1. Typical QLWFPC2 performance results with two WFPC2 observations of a Local Group globular cluster running on a 5-node Beowulf cluster with 1.8 GHz CPUs and a Gigabit-Ethernet local network. The points show actual run times for between 1 and 5 processors; QLWFPC2 running on 4 processors takes about 2.4 seconds. The thin line shows a simple performance model based on measured cluster performance metrics (network bandwidth, disk drive bandwidth, and execution time of QLWFPC2 with a single CPU). The thick line shows the theoretical limit of performance. Note that the current version of the QLWFPC2 algorithm already meets the ideal performance values for 1, 2, and 4 processors. A single WFPC2 data set is about 10 Mbytes in size and is partitioned into four calibrated images from the PC1, WF2, WF3, and the WF4 cameras; the current QLWFPC2 analysis algorithm sends all of the image data from one WFPC2 camera to a single compute (slave) node for analysis — the increase in computation time for 3 (5) processors compared to 2 (4) processors reflects the underlying 4-fold partitioning of a single WFPC2 data set. Spreading the analysis of data from a WFPC2 camera to all compute nodes would improve the computation time for 3 and 5 (and more) processors but would not improve the results for 1, 2 and 4 processors which are already optimal.

---

<http://www.noao.edu/staff/mighell/matphot/>

---

This work is/was supported by grants from the  
**National Aeronautics and Space Administration** ([NASA](#))

- Interagency Order No. NNG05EB61I (NRA 03-OSS-01)
- Interagency Order No. S-13811-G (NRA 01-OSS-01)

which were awarded by the  
**Applied Information Systems Research** ([AISR](#)) Program  
of NASA's [Science Mission Directorate](#).

---

## **MATPHOT: Stellar Photometry and Astrometry with Discrete Point Spread Functions**

- [Software](#) (Source code and documentation)
  - [MNRAS article describing the MATPHOT algorithm](#)
  - [Software](#) (Source code and documentation)
  - **Technology spinoff: MATPHOT interpolant ported to a Xilinx FPGA at the NCSA!**
  - [AAS 205 poster](#)
  - [AI2004 presentation](#)
- 

## **Stellar photometry and astrometry with discrete point spread functions**

**Mighell, K. J. 2005, [Monthly Notices of the Royal Astronomical Society](#), **316**, 861-878 (11 August 2005)**

The key features of the MATPHOT algorithm for precise and accurate stellar photometry and astrometry using discrete point spread functions (PSFs) are described. A discrete PSF is a sampled version of a continuous PSF, which describes the two-dimensional probability distribution of photons from a point source (star) just above the detector. The shape information about the photon scattering pattern of a discrete PSF is typically encoded using a numerical table (matrix) or an FITS (Flexible Image Transport System) image file. Discrete PSFs are shifted within an observational model using a 21-pixel-wide damped sinc function, and position-partial derivatives are computed using a five-point numerical differentiation formula. Precise and accurate stellar photometry and astrometry are achieved with undersampled CCD (charge-coupled device) observations by using supersampled discrete PSFs that are sampled two, three or more times more finely than the observational data. The precision and accuracy of the MATPHOT algorithm is demonstrated by using the c-language mpd code to analyse simulated CCD stellar observations; measured performance is compared with a theoretical performance model. Detailed analysis of simulated Next Generation Space Telescope observations demonstrate that millipixel relative astrometry and mmag photometric precision is achievable with complicated space-based discrete PSFs.

[Online MNRAS abstract](#)

[Online MNRAS article](#) (if a subscriber to MNRAS)

[PDF version of article](#) (... if not)

[astro-ph/0505455](#) ( [PDF](#) ) [astro-ph preprint](#)

---

## Technology spinoff: MATPHOT interpolant ported to a Xilinx FPGA at the NCSA!

The [National Center for Supercomputer Applications \(NCSA\)](#) and the [Ohio Supercomputer Center \(OSC\)](#) sponsored the [Reconfigurable Systems Summer Institute](#) which was held July 11--13, 2005 at the [Beckman Institute for Advanced Science and Technology](#) on the campus of the University of Illinois at Urbana-Champaign.

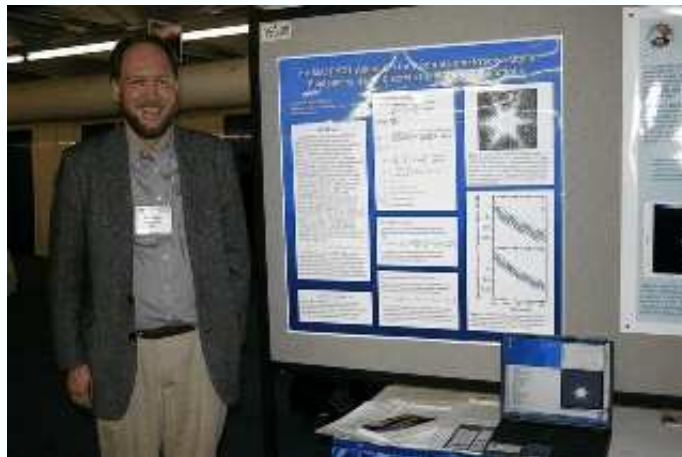
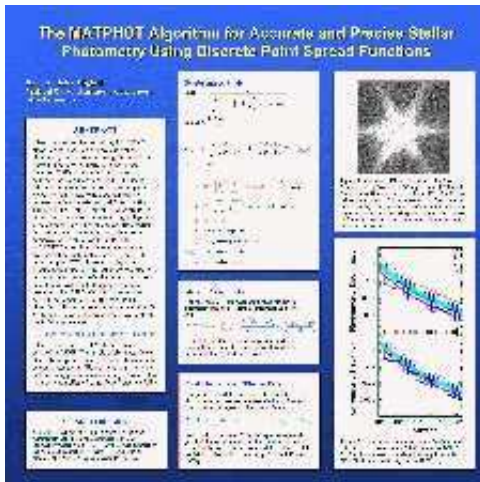
Volodymyr Kindratenko, a senior research scientist at NCSA, gave a presentation [First-hand experience on porting MATPHOT code to SRC platform](#) ( [PPT](#) ) ( [PDF](#) ) based on the MATPHOT code for stellar photometry and astrometry with discrete point spread functions.

Dr. Kindratenko analyzed the MATHOT code and determined that the current implementation spends approximately 90% of the total computation time calculating the two-dimensional damped sinc interpolation of PSF models. Kindratenko ported the C implementation of the interpolation algorithm to an [SRC MAPstation](#) which is based on SRC's patented [MAP processor](#) that has 2 [Xilinx](#) Field Programmable Gate Arrays ( [FPGAs](#) ).

---

[American Astronomical Society 205th Meeting poster #153.09](#)

2005 January 13, San Diego, CA



## The MATPHOT Algorithm for Accurate and Precise Stellar Photometry and Astrometry Using Discrete Point Spread Functions

[AAS abstract](#)

[ADS abstract](#)

**Mathematical Challenges in Astronomical Imaging**  
**Institute for Pure and Applied Mathematics**  
**2004 January 27, UCLA, Los Angeles, CA**



**[PDF version of the AI2004 poster](#)**

***Mathematical Challenges of using Point Spread Function Analysis Algorithms in Astronomical Imaging***  
**Ken Mighell (National Optical Astronomical Observatory)**

**[PDF version of the presentation](#)**

**MATPHOT release: 2005OCT28**

**Retrieve the MX source code file:**

- **MX source code gzipped tar ball:**  
**[mx\\_200510281613.tgz](#)**  
 (^- click the right mouse button on this link)

**Build MX (tested on Apple OS X Tiger and RedHat Linux 7.2):**

- **Unpack the tar ball by typing the following command:**  
**[zcat mx\\_200510281613.tgz | tar -xvf -](#)**
- **Go down to the new mx directory:**  
**[cd mx](#)**
- **Build MX:**  
**[make](#)**

**CHECK:** If the file **[bin/mx\\_mpd](#)** exists, you have built MATPHOT!

**Now try out MATPHOT:**

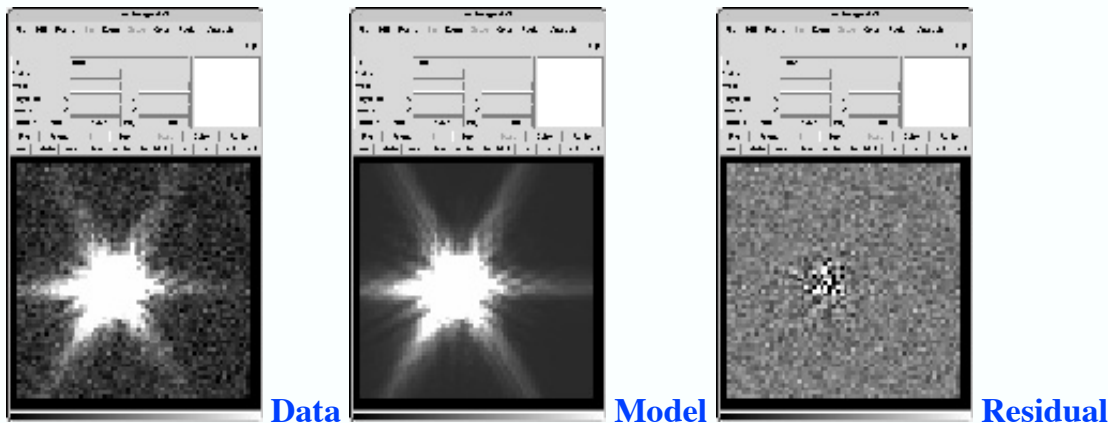
- **Go down to the src/mpd directory:**

[cd src/mpd](#)

- Type the following command:
  - [demos/ngst](#)  
and you will see MATPHOT analysis of 10 simulated *Next Generation Space Telescope* observations.
- Now start the [ds9](#) astronomical image display by typing the following command:
  - [ds9](#)

We can see the MATPHOT fitting process live using ds9 by typing the following command:

- [demos/ngst](#)



- We can simulate 20,000 NGST observations by typing the following commands:

- [demos/ngst\\_20000 > ngstx2 &](#)
- [tail -f ngstx2](#)

This will take a while...

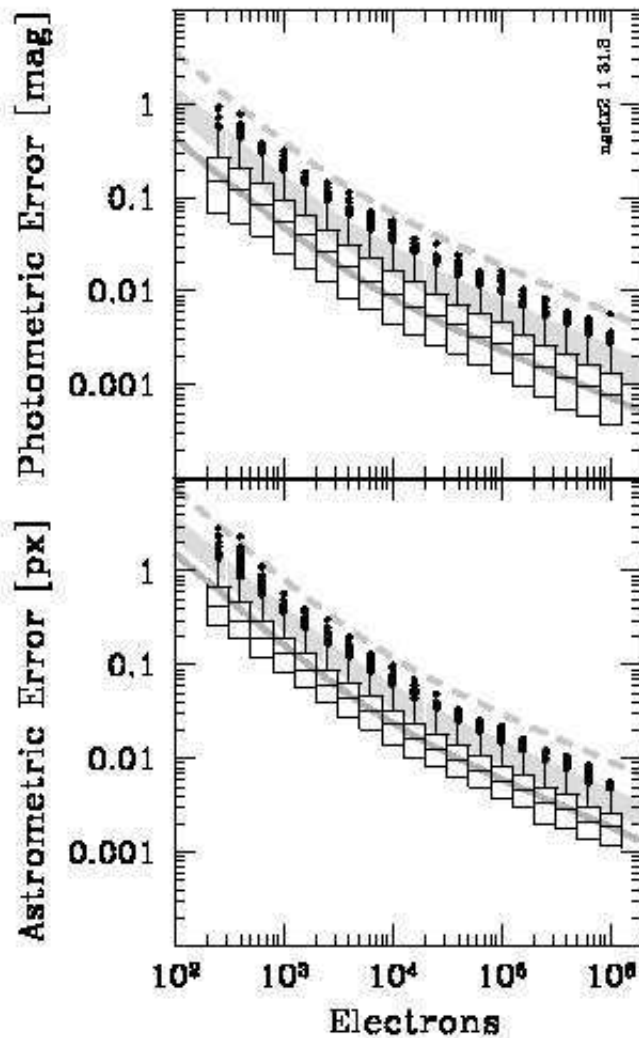
and will go faster if ds9 is not used to visualize the fitting process of all 20,000 stars :-)

When finished, use custom [SuperMongo](#) macros to look at the results by typing the following command:

- [sm/go ngstx](#)

The resultant plot should look like the following plot:





The grey lines are the predicted median values; the wide grey bands show the predicted top fence range of the box-and-whiskers plots; and the dashed grey lines show the predicted 5-sigma limits. This plot shows that millipixel relative astrometry and millimag photometric accuracy is achievable with very complicated space-based discrete Point Spread Functions. See the [AAS 205 poster](#) for more details.

More to come...

Kenneth Mighell  
Associate Scientist  
Kitt Peak National Observatory  
National Optical Astronomy Observatory

EMAIL: [mighell@noao.edu](mailto:mighell@noao.edu)

MAIL: P.O. Box 26732, Tucson, AZ 85726-6732

FEDEX: 950 N. Cherry Ave., Tucson, AZ 85719

PHONE: (520) 318-8391

**FAX:** (520) 318-8360

**URL:** <http://www.noao.edu/staff/mighell/>

---

**Last updated: 2005 October 28 @ 17:06 MST**

---

---

<http://www.noao.edu/staff/mighell/qlwfpc2>

---

## **QLWFPC2: Quick-Look WFPC2 Stellar Photometry based on the Message Passing Interface**

QLWFPC2 is a new parallel-processing stellar photometry code which is designed to do quick-look analysis of two entire WFPC2 observations from the Hubble Space Telescope in under 5 seconds using a fast Beowulf cluster with a Gigabit-Ethernet local network. This program is written in ANSI C and uses MPICH implementation of the Message Passing Interface from the Argonne National Laboratory for the parallel-processing communications, the CFITSIO library (from HEASARC at NASA's GSFC) for reading the standard FITS files from the HST Data Archive, and the Parameter Interface Library (from the INTEGRAL Science Data Center) for the IRAF parameter-file user interface. QLWFPC2 running on 4 processors takes about 2.4 seconds to analyze the WFPC2 archive datasets u37ga407r.c0.fits (F555W; 300 s) and u37ga401r.c0.fits (F814W; 300 s) of M54 (NGC 6715) which is the bright massive globular cluster near the center of the nearby Sagittarius dwarf spheroidal galaxy. The analysis of these HST observations of M54 lead to the serendipitous discovery of more than 50 new bright variable stars in the central region of M54. Most of the candidate variables stars are found on the PC1 images of the cluster center --- a region where no variables have been reported by previous ground-based studies of variables in M54. This discovery is an example of how QLWFPC2 can be used to quickly explore the time domain of observations in the HST Data Archive.

### QLWFPC2 Performance on a 5-node Beowulf Cluster

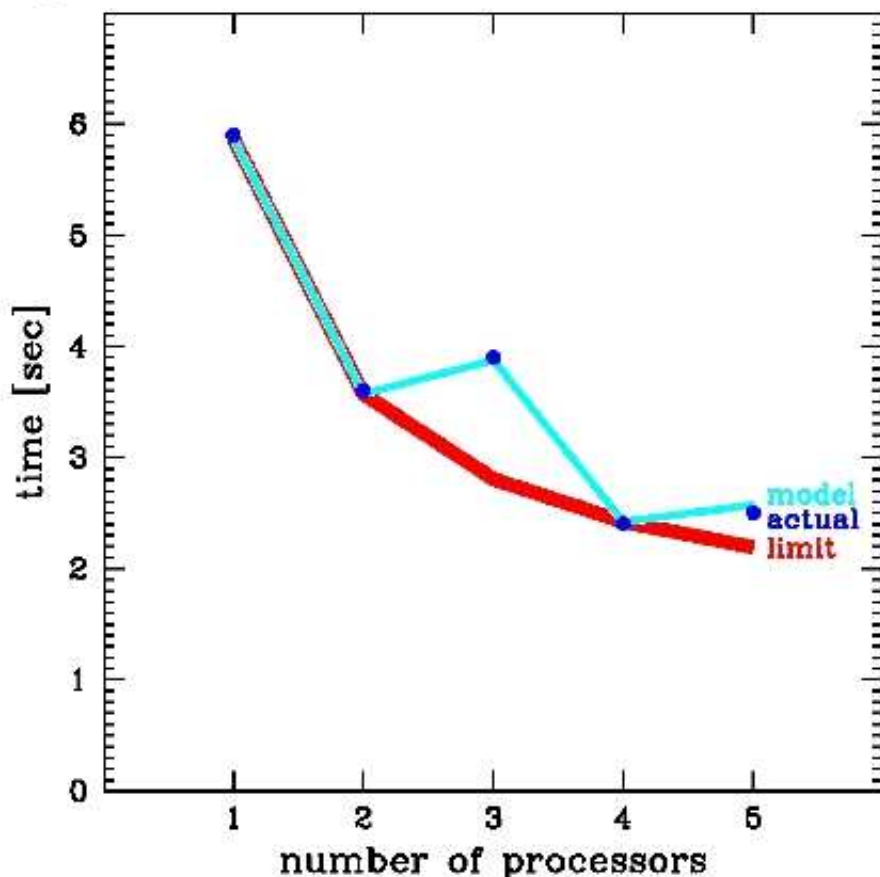


**Figure 1.** Typical QLWFPC2 performance results with two entire WFPC2 observations of a Local Group globular cluster running on a 5-node Beowulf cluster with 1.8 GHz CPUs connect with Gigabit Ethernet. The blue points show actual run times for 1 to 5 processors. The thin line shows a simple performance model based on measure cluster performance metrics (network bandwidth, disk I/O bandwidth, and performance with a single CPU). The thick line shows the theoretical limit of performance based on the system performance metrics. Note that the current version of QLWFPC2 already meets the ideal performance values for 1, 2, and 4 processors. QLWFPC2 running on 4 processors takes about 2.4 seconds to analyze the WFPC2 archive data sets u37ga407r.c0.fits (F555w; 300 s) and u37ga401r.c0.fits (F814w; 300 s) of M54 which is the bright massive globular cluster near the center of the nearby Sagittarius dwarf spheroidal galaxy. QLWFPC2 analyzed over 50,000 point source candidates and reported V, I, F555W, and F814W photometry of 14,611 stars with signal-to-noise ratios of 8 or better.

### ADASS XIII conference proceedings article:

- [adass2003\\_article.pdf](#) (PDF format)
- [adass2003\\_article.ps](#) (PostScript format)

### AAS 203rd Meeting, January 2004

Session 4 Computation, Data Handling and Image Analysis  
Poster, Monday, January 5, 2004, 9:20am-6:30pm, Grand Hall

### [4.01] QLWFPC2: Parallel-Processing Quick-Look WFPC2 Stellar Photometry

## based on the Message Passing Interface

*K. J. Mighell (National Optical Astronomy Observatory)*

I describe a new parallel-processing stellar photometry code called QLWFPC2 which is designed to do quick-look analysis of two entire WFPC2 observations from the Hubble Space Telescope in under 5 seconds using a fast Beowulf cluster with a Gigabit Ethernet local network. This program is written in ANSI/ISO C and uses the MPICH implementation of the Message Passing Interface from the Argonne National Laboratory for the parallel-processing communications, the CFITSIO library (from HEASARC at NASA's GSFC) for reading the standard FITS files from the HST Data Archive and the Parameter Interface Library (from the INTEGRAL Science Data Center) for the IRAF parameter-file user interface. QLWFPC2 running on 4 processors takes about 2.4 seconds to analyze WFPC2 archive datasets u37ga407r.c0.fits (F555W; 300 s) and u37ga401r.c0.fits (F814W; 300 s) of M54 (NGC 6715) which is the bright massive globular cluster near the center of the nearby Sagittarius dwarf spheroidal galaxy. The analysis of these HST observations of M54 lead to the serendipitous discovery of more than 50 new bright variable stars in the central region of M54. Most of the candidate variables stars are found on the PC1 images of the cluster center --- a region where no variables have been reported by previous ground-based studies of variables in M54. This discovery is an example of how QLWFPC2 can be used to quickly explore the time domain of observations in the HST Data Archive.

This work is supported by a grant from the National Aeronautics and Space Administration (NASA), Order No. S-13811-G, which was awarded by the Applied Information Systems Research Program (AISRP) of NASA's Office of Space Science (NRA 01-OSS-01).

If you would like more information about this abstract, please follow the link to <http://www.noao.edu/staff/mighell/qlwfpc2>.

### 203rd AAS meeting poster:

- [aas203\\_poster.pdf](#) (PDF format)
- [aas203\\_poster.ppt](#) (Microsoft PowerPoint format)

---

QLWFPC2 release: **2005OCT28**

### [Retrieve and build MX](#)

(^ click on this link and follow the instructions)

### Build QLWFPC2:

- From the main mx directory, go down to the src/qlwfpc2/src directory:

`cd src/qlwfpc2/src`

- QLWFPC2 uses the [Message Passing Interface \(MPI\)](#) standard, so in order to build QLWFPC2, **you will need to have a working implementation of MPI with a mpicc compiler command on your machine.**

- Assuming that you have mpicc working on your machine...  
build QLWFPC2 by typing the following command:

`make`

**CHECK:** If the file `../bin/qlwfpc2` exists, you have built QLWFPC2!

### Now try out QLWFPC2:

- The simplest invocation with one processor:
  - Type the following command:

[./qlwfp2](#)

and accept the default values for the first and second WFPC2 image filenames.  
The program output is found in the following files:

[.qlwfp2imag1](#)  
[.qlwfp2imag2](#)  
[.qlwfp2imag1.xml](#)  
[.qlwfp2imag2.xml](#)

- Same results using the mpirun command:
  - Type the following command:  
[mpirun -np 1 qlwfp2](#)
- Now give the names of the images on the command line:
  - Type the following command:  
[mpirun -np 1 qlwfp2 data/v1.fits data/i1.fits](#)  
Note that you are no longer prompted for the name of the WFPC2 image files.
- If you want to be verbose...
  - Type the following command:  
[mpirun -np 1 qlwfp2 image1=data/v1.fits image2=data/i1.fits](#)
- Now try QLWFPC2 with 4 processors:
  - Type the following command:  
[mpirun -np 4 qlwfp2 data/v1.fits data/i1.fits](#)  
The reported elapsed time should have gone down significantly :-)  
--- if mpirun has access to 4 processors!

## More to come...

---

This work is supported by a grant from the  
[National Aeronautics and Space Administration \(NASA\)](#),  
Order No. S-13811-G, which was awarded by the  
Applied Information Systems Research Program (AISRP)  
of NASA's Office of Space Science (NRA 01-OSS-01).

---

Kenneth Mighell  
Associate Scientist  
Kitt Peak National Observatory  
National Optical Astronomy Observatory

EMAIL: [mighell\\_at\\_noao\\_dot\\_edu](mailto:mighell_at_noao_dot_edu)  
MAIL: P.O. Box 26732, Tucson, AZ 85726-6732  
FEDEX: 950 N. Cherry Ave., Tucson, AZ 85719  
PHONE: (520) 318-8391  
FAX: (520) 318-8360  
URL: <http://www.noao.edu/staff/mighell/>

---

Updated: 2005 October 28 @ 17:05 MST